Earth and Space Science

DATA ARTICLE
10.1029/2023EA003076

Seasonal Distribution of Gravity Waves Near the Stratopause in 2019–2022

Shuang Xu[1], Justin N. Carstens[2], Jeff A. France[3], Cora E. Randall[4,5], Jia Yue[6,7], V. Lynn Harvey[4,5], Jie Gong[7], Jerry Lumpe[8], Lars Hoffmann[9], and James M. Russell III[1]

[1]Department of Atmospheric and Planetary Sciences, Hampton University, Hampton, VA, USA, [2]Bradley Department of Electrical and Computer Engineering, Virginia Polytechnic Institute and State University, Blacksburg, VA, USA, [3]White Ridge Solutions LLC, Frederick, MD, USA, [4]Laboratory for Atmospheric and Space Physics, University of Colorado Boulder, Boulder, CO, USA, [5]Department of Atmospheric and Oceanic Sciences, University of Colorado Boulder, Boulder, CO, USA, [6]Physics Department, Catholic University of America, Washington, DC, USA, [7]NASA Goddard Space Flight Center, Greenbelt, MD, USA, [8]Computational Physics, Inc., Boulder, CO, USA, [9]Jülich Supercomputing Centre, Forschungszentrum Jülich, Jülich, Germany

Key Points:

- Aeronomy of Ice in the Mesosphere cloud imaging and particle size (CIPS) provides first near-global images of gravity waves at 50–55 km with high horizontal resolution
- CIPS observes gravity wave hotspots generated by convection, topography, and the polar vortex
- Locations of gravity wave hotspots near the stratopause/lowermost mesosphere are similar to those in the mid-stratosphere near 35 km

Supporting Information:

Supporting Information may be found in the online version of this article.

Correspondence to:

S. Xu,
xushuang9999@gmail.com

Citation:

Xu, S., Carstens, J. N., France, J. A., Randall, C. E., Yue, J., Harvey, V. L., et al. (2024). Seasonal distribution of gravity waves near the stratopause in 2019–2022. *Earth and Space Science*, *11*, e2023EA003076. https://doi.org/10.1029/2023EA003076

Received 31 MAY 2023
Accepted 4 DEC 2023

Author Contributions:

Conceptualization: Shuang Xu, Justin N. Carstens, Jeff A. France, Cora E. Randall, V. Lynn Harvey
Data curation: Justin N. Carstens, Jeff A. France, Cora E. Randall, V. Lynn Harvey, Jerry Lumpe
Formal analysis: Shuang Xu, Justin N. Carstens, Jeff A. France, Cora E. Randall, Jia Yue, V. Lynn Harvey
Funding acquisition: Cora E. Randall, James M. Russell III

Abstract The cloud imaging and particle size (CIPS) instrument onboard the Aeronomy of Ice in the Mesosphere satellite provides images of gravity waves (GWs) near the stratopause and lowermost mesosphere (altitudes of 50–55 km). GW identification is based on Rayleigh Albedo Anomaly (RAA) variances, which are derived from GW-induced fluctuations in Rayleigh scattering at 265 nm. Based on 3 years of CIPS RAA variance data from 2019 to 2022, we report for the first time the seasonal distribution of GWs entering the mesosphere with high (7.5 km) horizontal resolution on a near-global scale. Seasonally averaged GW variances clearly show spatial and temporal patterns of GW activity, mainly due to the seasonal variation of primary GW sources such as convection, the polar vortices and flow over mountains. Measurements of stratospheric GWs derived from Atmospheric InfraRed Sounder (AIRS) observations of 4.3 μm brightness temperature perturbations within the same 3-year time range are compared to the CIPS results. The comparisons show that locations of GW hotspots are similar in the CIPS and AIRS observations. Variability in GW variances and the monthly changes in background zonal wind suggest a strong GW-wind correlation. This study demonstrates the utility of the CIPS GW variance data set for statistical investigations of GWs in the lowermost mesosphere, as well as provides a reference for location/time selection for GW case studies.

1. Introduction

Gravity waves (GWs) can be excited when perturbed air parcels are restored to equilibrium by buoyancy and gravity in a stably stratified atmosphere. GWs are commonly manifested in spatial and temporal variations in temperature, wind, and gas densities. The primary sources of atmospheric GWs include winds over orography (Holton, 1992), convection (e.g., Alexander et al., 1995), and imbalances in jet/frontal systems (e.g., Wu & Zhang, 2004). Secondary and less frequently occurring sources of GWs include wind shear (Fritts, 1982), wave-wave interactions (Wüst & Bittner, 2006), body forces accompanying wave dissipation (Vadas et al., 2003), tsunamis (Garcia et al., 2014), and volcanos (Yue et al., 2022). Given suitable propagation conditions, GWs can transfer significant energy and momentum from one region to another, both horizontally and vertically. They are the main drivers of many well-known global scale phenomena, for example, the quasi-biennial oscillation (Baldwin et al., 2001) and the pole-to-pole mesospheric residual circulation (Holton, 1982). Therefore, GWs play an important role in atmospheric coupling and shaping the global circulation, especially in the stratosphere and layers above. Furthermore, as our society substantially relies on satellite-based technologies such as the global navigation satellite system, there are increasing demands for accurate forecasting of space weather in the ionosphere-thermosphere-mesosphere (ITM) system. As the stratopause (at an altitude of ∼50 km) is the "gateway" to the ITM, the GW climatological distribution near the stratopause and lowermost mesosphere has drawn increasing interest among the science community (Forbes et al., 2021). In this article, we focus on the GWs at or just above the stratopause observed by the cloud imaging and particle size (CIPS) instrument (McClintock et al., 2009) on board the Aeronomy of Ice in the Mesosphere (AIM) satellite (Russell et al., 2009) and discuss their seasonal distributions.

One motivation to understand GWs near the stratopause observed by a satellite-based instrument is to constrain parameterizations of GW effects for numerical models. With the advances in theoretical physics and computing

Investigation: Shuang Xu, Cora E. Randall, Jia Yue, V. Lynn Harvey, Jie Gong, Lars Hoffmann
Methodology: Shuang Xu, Justin N. Carstens, Jeff A. France, Cora E. Randall, V. Lynn Harvey
Project Administration: Cora E. Randall, Jia Yue, V. Lynn Harvey, James M. Russell III
Resources: Cora E. Randall, V. Lynn Harvey, Jie Gong, Jerry Lumpe, Lars Hoffmann, James M. Russell III
Software: Justin N. Carstens, Jerry Lumpe, Lars Hoffmann
Supervision: Cora E. Randall, Jia Yue, V. Lynn Harvey, James M. Russell III
Validation: Shuang Xu, Justin N. Carstens, Jeff A. France, Cora E. Randall, Jia Yue, Jie Gong, Lars Hoffmann
Visualization: Shuang Xu, Justin N. Carstens, Jeff A. France, V. Lynn Harvey, Jerry Lumpe
Writing – original draft: Shuang Xu
Writing – review & editing: Justin N. Carstens, Jeff A. France, Cora E. Randall, Jia Yue, V. Lynn Harvey, Jie Gong, Jerry Lumpe, Lars Hoffmann, James M. Russell III

technology, scientists can now successfully simulate major atmospheric features via contemporary numerical weather prediction and climate models. However, significant portions of GWs are unresolved or under-resolved in conventional climate models and some numerical weather prediction models due to limited spatiotemporal resolution. Unresolved GWs must be parameterized to compensate for underrepresented GW effects, in order to enable accurate climate simulations (Kruse et al., 2023). However, these parameterizations are often ad hocly implemented without sufficient observational constraints. Among all observation techniques, satellite-based observations are the only type that can achieve repeating global observations with relatively high temporal frequency. Although each satellite-based instrument has limitations in spatial resolution and tends to be sensitive only to some portion of the GW spectrum, global characterization of GWs from a satellite observation data set is still an important reference to constrain and verify GW parameterizations in numerical models.

Evaluation of the collective impact of GWs on atmospheric coupling requires extensive analysis of observations from various instruments for different altitudes on a wide range of temporal and spatial scales (e.g., Alexander & Barnet, 2007). Limb measurements (e.g., the sounding of the atmosphere using broadband emission radiometry (SABER), microwave limb sounder (MLS) and High-Resolution Dynamics Limb Sounder (HIRDLS)) have high vertical range and resolution, but they cannot directly provide GW information on small horizontal scales (Ern et al., 2011; Meyer et al., 2018; Wright et al., 2016). On the contrary, nadir measurements (e.g., the Atmospheric Infrared Sounder (AIRS) and the Visible Infrared Imaging Radiometer Suite (VIIRS)) have high horizontal resolution but cannot capture small-scale perturbations in the vertical dimension directly (Hoffmann et al., 2013; Miller et al., 2018; Yue et al., 2019). With 7.5-km horizontal resolution, CIPS belongs to the second group. It is the first nadir-looking satellite instrument to make near-global observations of GWs entering the ITM.

CIPS observations of Rayleigh scattering at a wavelength of 265 nm are used to derive the Rayleigh Albedo Anomaly (RAA) data set, from which GWs at an altitude of ~50–55 km are inferred (Randall et al., 2017). This data set has since been used in various GW studies. For example, Kogure et al. (2021) used CIPS RAA data to investigate the reason for a decline in GW activity in the middle/upper atmosphere after the rare Antarctic SSW in 2019. Wright et al. (2022) used CIPS RAA images to show GWs that propagated to the mesosphere 12 hr after the January 2022 Tonga volcano eruption, 12,300 km away from the source. Forbes et al. (2022, 2021) employed CIPS RAA variance data to investigate GWs in the mid- and low-latitudes in regions during the monsoon (summer solstice) seasons. The monthly/seasonal variations in this article are the first to show GW activity near altitudes of 50–55 km near-globally in all seasons. In order to find local maxima or "hotspots" of GW activity, we also derive the CIPS peak event frequencies (PEFs) using the method initially introduced by Hoffmann et al. (2013) for AIRS 4.3 µm brightness temperature (BT) variances. Here we compare CIPS RAA variances to AIRS BT variances within the same time range. We discuss the similarities and differences between the results derived from the two data sets, then investigate possible causes for the differences.

The article is arranged as follows: in Section 2, we describe the CIPS instrument, the methodology to derive the RAA variance data set, the AIRS data set, and the meteorological reanalysis data used in this work. In Section 3, we compare the near-global statistical (seasonal/monthly) results obtained from CIPS RAA and AIRS 4.3 µm BT variances. In Section 4, we present some significant GW hotspots observed in the RAA variance data set and compare with AIRS. Finally, Section 5 provides conclusions and a future outlook.

2. Data and Analysis Methods

2.1. CIPS RAA and RAA Variance

NASA's AIM satellite was launched into orbit from a Pegasus XL rocket on 25 April 2007. It was the first satellite mission dedicated to and designed for the study of polar mesospheric clouds (PMCs) near the summer mesopause, about 83 km above the Earth's surface. The AIM satellite is in a nearly circular, sun-synchronous orbit at 600 km altitude. The local solar time (LST) of the ascending node is slowly drifting (Russell et al., 2009). The CIPS instrument is a panoramic ultraviolet (UV) imager operating in a 10-nm passband centered at 265 nm. Data are collected using four cameras arranged to create a bowtie-shaped field of view (FOV) referred to as a "scene." The FOV projected to the Earth's surface is 1,000 × 2,000 km in the sub-satellite direction. The horizontal resolution of pixels in each camera can reach 1 × 2 km for small viewing angles, but the resolution degrades near the edge of the FOV as viewing angle increases. Hence, the RAA and RAA variance data are binned to 7.5 × 7.5 km to achieve a uniform resolution.

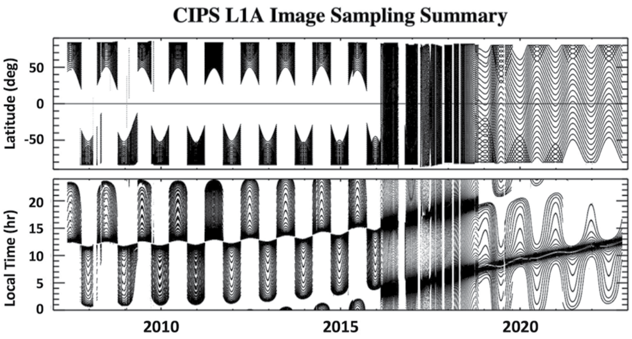

Figure 1. Mean latitude (top) and local time (bottom) for all cloud imaging and particle size (CIPS) level 1A images from the PY camera from May 2007 through October 2022. Each individual level 1A image is represented by a black dot. More than 2.2 million individual images are represented by dots in these plots.

The CIPS instrument was designed primarily to monitor PMCs by measuring the 265-nm radiation scattered by PMCs, which appears as an enhancement to the background Rayleigh scattering from atmospheric N_2 and O_2. In the absence of PMCs, the Rayleigh scattered radiation detected by CIPS is controlled by variations in the neutral density and ozone absorption along the line-of-sight, with a source function peak near 50–55 km altitude (Bailey et al., 2009; McPeters, 1980). Therefore, coherent perturbations in the CIPS observations are generally indicative of variations in the neutral and/or ozone density induced by GWs near 50–55 km. Due to its combined horizontal resolution and FOV, CIPS can capture GWs with horizontal wavelengths on scales from tens to hundreds of kilometers. The variations of interest are quantified by the RAA, the residual difference between the observed Rayleigh scattering albedo and a "baseline" albedo, expressed as %. The "baseline" albedo is defined as the albedo in the absence of any small-scale atmospheric variations, which is calculated using the observation geometry of each CIPS pixel and a numerical generalization of the "C-σ" model. The "C-σ" model is an analytical model that describes the Rayleigh scattering background albedo, where the C parameter refers to the phase adjusted albedo for an air parcel viewed in the nadir at the subsolar point, and σ is the ratio of the ozone scale height to the atmospheric scale height (Carstens et al., 2013; Randall et al., 2017). With these measurements, CIPS provides a unique view of atmospheric coupling through observations of GWs at or just above the stratopause.

Figure 1 shows the mean latitude and local time for all PY camera level 1A (calibrated and geolocated) images for the time period from the AIM launch in May 2007 until October 2022. The PY camera is one of two cameras that are primarily nadir oriented (see Figure 1 in Lumpe et al., 2013); latitude and local time sampling of the other three cameras is similar to that of the PY camera. The upper panel in Figure 1 shows that before February 2016 CIPS only sampled latitudes from ~20° to 50° to the pole in the spring and summer hemispheres. In March of 2016 CIPS began observing all sunlit latitudes year-round, facilitating a near-global seasonal study of GWs at (or just above) the stratopause.

The RAA variance is derived from the level 2A RAA data, which consists of individual four-camera "scenes," wherein simultaneous images in the four overlapping cameras are merged seamlessly (e.g., see Figures 1 and 2 in Randall et al., 2017). Each level 2A scene is converted to wavenumber space by a fast Fourier transform (FFT). Any wave structures with horizontal wavelength $\lambda_H < 20$ km (~three pixels) or $\lambda_H > 400$ km are removed by the ninth-order Butterworth filters. The filtering is conducted both along and across track. Although CIPS is capable of detecting GWs with horizontal wavelengths from 15 to 600 km (or longer if successive scenes are aligned favorably), characterization of RAA variance for GWs with wavelengths longer than 400 km is compromised by low signal-to-noise ratios (SNRs). Figure 2a shows the bandpass response curve of the applied Butterworth bandpass filter. Figure 2b shows the raw RAA data for one scene.

To characterize the influence of noise in the wave analysis, we introduce the spectral amplitude SNR:

$$\text{Spectral Amplitude SNR} = \frac{\text{spectral amplitude}}{\text{median noise level}}. \tag{1}$$

The spectral amplitude SNR in Equation 1 is calculated for each spectral component in a given scene, where spectral component refers to the horizontal vector wavenumber; that is, 1/wavelength and horizontal phase speed direction. Note that the sign of the wave propagation direction cannot be determined, so there is a 180° ambiguity in the direction. The numerator in Equation 1 is the magnitude (absolute value) of the complex FFT output for the spectral component of interest. The denominator is calculated from an empirical model of the noise. This model is derived using a set of 42 wave-free orbits during periods of quiet GW activity in April 2020, for which the observed RAA variance can be attributed solely to noise. The denominator in Equation 1 is thus defined as the median RAA variance over the set of wave-free scenes, for the spectral component in question. Figure 2c shows an example of how the spectral amplitude SNR varies with wavenumber and phase speed direction over a single scene. That is, Figure 2c can be interpreted as a polar coordinate plot where the wavelength (1/wavenumber, in km) is represented by the radial distance and the phase speed direction is represented by the radial angle. This angle is defined relative to the coordinate system of the scene as depicted in Figure 2b. Thus 0° denotes horizontal propagation (wavefronts oriented vertically) and 90° denotes vertical propagation (wavefronts oriented horizontally), where vertical and horizontal refer to the planar geometry in Figure 2b. Those spectral components with spectral amplitude SNR less than 1.7 are considered insignificant and are denoted by the diagonal lines (hatched region) in Figure 2c. The threshold of 1.7 was determined empirically by sensitivity studies that indicated this value conservatively limits the probability that noise would be detected as a wave to no worse than 1-in-1,000.

Figure 2d shows the filtered RAA, which is calculated by inverting the FFT data back to the spatial domain after removing all insignificant spectral components (hatched region in Figure 2c). The diagonal lines in Figure 2d indicate that the RAA variance SNR <3, where the variance SNR is defined for each spatial pixel as the filtered RAA variance divided by the uncertainty (noise) in the filtered RAA variance:

$$\text{Variance SNR} = \frac{\text{Filtered RAA variance}}{\text{Filtered RAA variance uncertainty}}. \tag{2}$$

The filtered RAA variance for a given pixel is the variance of the filtered RAA data in all pixels that are within a radius of 155 km of the targeted pixel. Calculating the filtered RAA variance uncertainty for a given pixel, or noise in the filtered RAA variance, requires identifying the noise due to only the retained (significant) spectral components. Furthermore, since the noise due to individual spectral components is calculated in the spectral domain as described above, calculating the denominator in Equation 2 requires converting from the spectral to the spatial domain. This conversion is accomplished by first calculating a spectral-to-spatial conversion factor, F, equal to the fraction of the noise permitted through the filter:

$$F = \frac{\sum\limits_{(\text{significant } k)} \nu_k}{\sum\limits_{(\text{all } k)} \nu_k}. \tag{3}$$

Here, k is an index over all spectral components, and ν_k is the median noise level (denominator in Equation 1) for each spectral component, k. Unlike the wave packets, noise in the filtered RAA variance is not localized in the spatial domain to the wave region responsible for creating the spectrally significant amplitudes. Instead, noise in the filtered RAA variance is spread throughout the whole scene and tends to maintain the envelope of the unfiltered noise field, with greater noise levels near the edges of the scene where the native resolution is lower and background Rayleigh albedo is higher. Therefore, the noise field permitted through the filter is estimated by multiplying the square of the RAA variance in each pixel by F. Finally, the filtered noise field is smoothed over the surrounding 155-km pixel region, yielding the filtered RAA variance uncertainty in the targeted pixel. Figure 2e shows the filtered RAA variance ($\%^2$) for the regions where variance SNR >3 (i.e., the regions without diagonal lines in Figure 2d). Images like Figures 2b–2e for each scene are produced regularly as part of the available CIPS data products (see Acknowledgments).

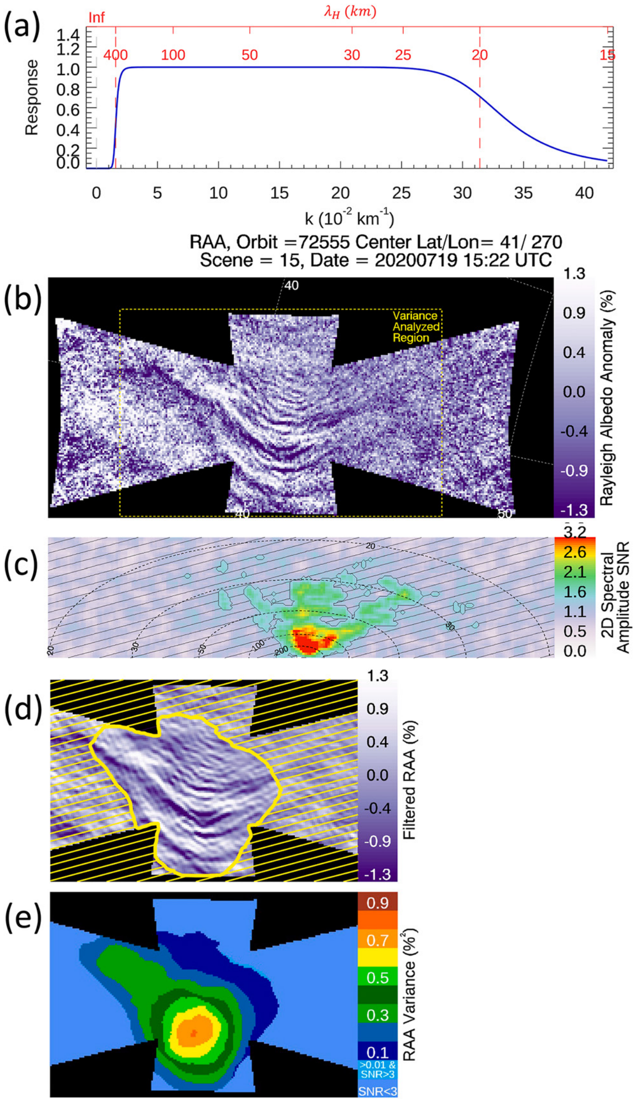

Figure 2. (a) Bandpass response curve of the bandpass filter for each scene; (b) a sample scene of "raw" cloud imaging and particle size (CIPS) Rayleigh Albedo Anomaly (RAA) observations; (c) 2D spectral amplitude signal-to-noise ratio (SNR) of the sample scene in (b) via forward fast Fourier transform (FFT) including only the region inside the dotted yellow line in (b); diagonal lines denote areas with spectral amplitude SNR <1.7, X and Y coordinates correspond to wavenumber ($2\pi/\lambda$, where λ is denoted by dotted black contours in unit of km); (d) filtered RAA, reconstructed from the FFT back into the spatial domain, after filtering spectral components with spectral amplitude <1.7; diagonal lines denote variance SNR <3; (e) CIPS RAA variance; all values for which variance SNR <3 are denoted by the lowest color bar level.

2.2. AIRS BTs and Variance

Here we compare CIPS measurements to AIRS 4.3 μm BT perturbation data. Figure 3 depicts the normalized weighting functions for the 4.3-μm emission observed by AIRS and the 265-nm Rayleigh scattering observed

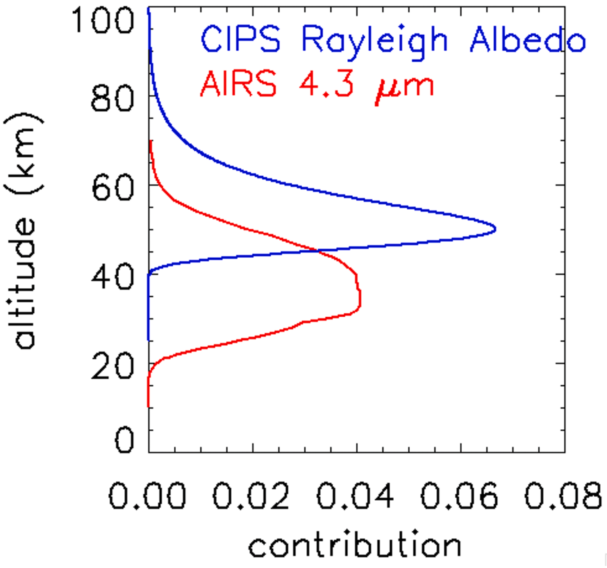

Figure 3. The contribution functions of cloud imaging and particle size (CIPS) 265 nm Rayleigh albedo (blue) and Atmospheric InfraRed Sounder (AIRS) 4.3 μm brightness temperature channel (red).

by CIPS. The AIRS kernel function has a broad peak centered near 35 km altitude (Hoffmann & Alexander, 2010), about 15 km lower in altitude than that of CIPS. Hoffmann et al. (2013) used the AIRS 4.3 μm BT variance data set to show the seasonal and global variability of stratospheric GWs. For purposes of the comparisons presented here, the CIPS RAA variance can be treated as a variable roughly proportional to temperature variance due to GWs near an altitude of 50 km (Forbes et al., 2021). The important parameters introduced in Section 2.1 are optimized for the CIPS measurements and RAA variance data set, which are in many ways different from the parameters that were used for deriving AIRS variance. Table 1 provides a quick reference to crucial parameters used for deriving the RAA data set and AIRS 4.3 μm BT perturbation data set. See Hoffmann and Alexander (2010) and Hoffmann et al. (2013) for more details on the AIRS 4.3 μm BT perturbation data.

The orbit strip width (fifth row in Table 1) is an important parameter in understanding differences in statistical studies of RAA and AIRS. A wider swath leads to more overlap between the measurements on adjacent orbits, enabling higher temporal-resolution in areas of interest. Accordingly, the CIPS measurements have lower temporal-resolution, because the orbit strips are only 500–850 km wide, ~1/3 of the AIRS orbit strip width. As the orbital periods of CIPS and AIRS are almost the same (~95 min for CIPS vs. ~99 min for AIRS), at low latitudes it takes CIPS 3 times longer to accumulate the same number of observations as AIRS at a given location. Another salient difference between the RAA and AIRS variance data sets is the schemes for GW extraction. The AIRS 4.3 μm BT perturbation variances are defined by differencing the BT perturbations from a smooth background that is characterized by a fourth-order polynomial fit (Hoffmann et al., 2013). The CIPS RAA variances, on the other hand, are defined by FFT wave filtering. All parameters in Table 1 contribute to differences between the CIPS and AIRS GW statistical results discussed in the next section.

Section 3 compares statistical results of GWs derived from the CIPS and AIRS observations in the ascending orbits, as both data sets have LST near noon at the ascending nodes. Hoffmann et al. (2014) point out that the daytime scene temperatures are up to 10 K higher than the nighttime values as the CO_2 molecules experience solar excitation and enter the state of non-local thermodynamic equilibrium. As a result, the noise and variance in AIRS 4.3 μm nighttime observations are higher. The AIRS ascending orbit strips partially stretch toward or into the night side across the day-night terminator in high latitudes, which may induce higher variance at the polar caps. Hence, we excluded the data in all pixels for which the solar zenith angle (SZA) >76.5° so as not to mislead the reader into thinking that the GW variance is higher there. Similarly, when processing the AIRS 4.3 μm BT nighttime observations (see Figure S1 in Supporting Information S1), we omitted the data in all pixels for which the SZA <103.5°, since the variances in the polar summer region at these SZA values are biased low.

As a hyperspectral infrared spectrometer, AIRS also has channels around 15 μm, some of which can be used to retrieve the BT peaks at ~40 km altitude (Gong et al., 2012). The 15-μm weighting function peak altitude matches the CIPS weighting function peak altitude better than that of the 4.3-μm weighting function, but the 4.3 μm data are used in this study for its better quality and much reduced noise (Hoffmann et al., 2014), as the altitude range mismatch is a lesser factor. Nevertheless, the GW monthly results at ~40 km altitude based on AIRS 15 μm BT perturbation can still be found in the Figure S2 in Supporting Information S1. (Note that the lower limit of the color scale in Figure S2 in Supporting Information S1 is very high because of the high noise level in the AIRS 15 μm BT perturbation data set.) If not specified, the term "AIRS" in the following sections refers to AIRS observations in the 4.3-μm bands, not the 15-μm bands.

2.3. The Modern-Era Retrospective Analysis for Research and Applications, Version 2 (MERRA-2)

Modern-Era Retrospective Analysis for Research and Applications, Version 2 (MERRA-2) reanalysis (Bosilovich et al., 2015; Molod et al., 2015) is used in this work to provide information on the background wind field to aid in the interpretation of CIPS and AIRS GW variance observations. The reanalysis data are taken four times daily with a horizontal resolution of 0.5° latitude by 0.625° longitude on 72 model levels that extend from

Table 1
Parameters and Scheme for Deriving Cloud Imaging and Particle Size (CIPS) Rayleigh Albedo Anomaly (RAA) Variance Data Set and Atmospheric InfraRed Sounder (AIRS) Brightness Temperature (BT) Perturbation Data Set

Instrument	CIPS	AIRS
Type of radiance measured by instrument	Nadir-sounding UV Rayleigh scattering, λ = ~265 nm	Nadir-sounding thermal infrared emission, λ = ~4.3 μm
Footprint size	56.25 km^2 (7.5 km × 7.5 km), nearly uniform for RAA variance	From 182.25 km^2 (13.5 km × 13.5 km) at nadir to 877.4 km^2 (41 km × 21.4 km) at scan extremes
Altitude of instrument	~600 km	~700 km
Altitudes for GWs	50–55 km	30–40 km
Width of orbit strip	500–850 km	1,780 km
Variables of data set that contain GW information	RAA (unit: %) and RAA variance (unit: %^{2})	BT perturbation (unit: K) and BT variance (unit: K^2)
Method to extract GWs	FFT wave filtering based on RAA of each scene in wavenumber space	Differences from fourth-order polynomial fit of BT values for each scan
Horizontal and vertical wavelengths of detectable GWs (λ_H and λ_z)	$\lambda_H = 30$–400 km $\lambda_z > 15$ km (Carstens et al., 2014)	$\lambda_H = 50$–900 km $\lambda_z > 12$ km (Hoffmann et al., 2014)
Radius of local neighborhood for calculating variances	155 km	100 km
Approximate LST at equator	Drifting from 08:00 (April 2019) to 12:00 (March 2022) at ascending nodes, only daytime (see Figure 1)	~01:30 for descending nodes and ~13:30 for ascending nodes

the Earth's surface to 0.01 hPa (~75 km) (Global Modeling and Assimilation Office (GMAO), 2015). This reanalysis assimilates MLS temperature and ozone above 5 hPa beginning in August 2004 (Gelaro et al., 2017) to better constrain the dynamics in the upper stratosphere and lower mesosphere. In this work, we only use wind averages in a certain UT range according to the locations of interest so that the corresponding local times over each location are close to the local times when CIPS and AIRS observe for each day. The reanalysis data are linearly interpolated to a 2° latitude by 2.5° longitude grid and to potential temperature levels ranging from 300 K (~10 km) to 4,600 K (~75 km). For this work, MERRA-2 zonal wind is averaged over the 800–1,400 K (~30–40 km) potential temperature levels for comparison to AIRS and from 2,000 to 2,400 K (50–55 km) for comparison to CIPS.

3. Statistical Results Based on CIPS and AIRS Observations

3.1. Seasonal GW Variances in CIPS and AIRS

Figure 4 shows the inter-comparison of seasonally averaged GW variance distribution based on 3 years of observations derived from the CIPS RAA and AIRS 4.3 μm BT data from April 2019 to March 2022. The definition of four seasons in Figure 4 follows Hoffmann et al. (2013), that is, November–February (NDJF), March and April (MA), May–August (MJJA), and September and October (SO). For CIPS RAA results in Figure 4, the statistical analysis uses a total of 3.751×10^9 valid pixels. The global equidistant cylindrical maps are gridded every 0.5° in longitude and latitude. The averaged variance and number of pixels within each map grid point are calculated. Grid points with less than 280 pixels per month are plotted in gray. The reason for setting 280 pixels as a threshold for presenting results is explained in caption of Figure S4 in Supporting Information S1. The red cross-hatched regions from 50°S to 90°S (southern summer) in Figure 4a and from 50°N to 90°N (northern summer) in Figure 4c reveal unphysically high RAA variances due to the contamination of the RAA retrievals from PMC scattering. Compared to the seasonal grid-averaged AIRS 4.3 μm BT variances in the same observation time range (Figure 5), the CIPS RAA counterparts indicate a similar distribution pattern but a higher contrast between the GW and non-GW regions. Although the units for CIPS RAA variances (%^{2}) and AIRS BT variances (K^2) are different, the higher contrast in RAA variances can be attributed mainly to the higher zonal wind at stratopause altitudes than in the stratosphere below and higher SNR in the RAA signal. More discussion about the comparison between GW variances in RAA and AIRS in specific regions is in Section 4.

Figure 4 shows that results from both CIPS and AIRS indicate large regions with elevated GW activity in NDJF (panels a and e) and MJJA (panels c and g). In the summer hemisphere, there is a three-peak structure in GW variances in the subtropics related to convective sources associated with the summer monsoons (Forbes et al., 2021, 2022). These occur over the east coasts of South America, southern Africa, and the Australia-Pacific region during austral summer (panels a and e), and over the east coast of north America, northern Africa, and South Asia-Pacific region during boreal summer (panels c and g). In the winter hemisphere, GWs are ubiquitous in mid-latitudes due to flow over terrain (e.g., Lott & Miller, 1997; Mcfarlane, 1987) and/or unbalanced jet streams (e.g., Plougonven & Zhang, 2014; Plougonven et al., 2017). The high GW activity between 30° and 60° latitude in the winter hemisphere during NDJF and MJJA can be explained by the prevailing zonal wind profile during those seasons (see Harvey et al., 2023). Throughout the stratosphere in mid- and high-latitudes,

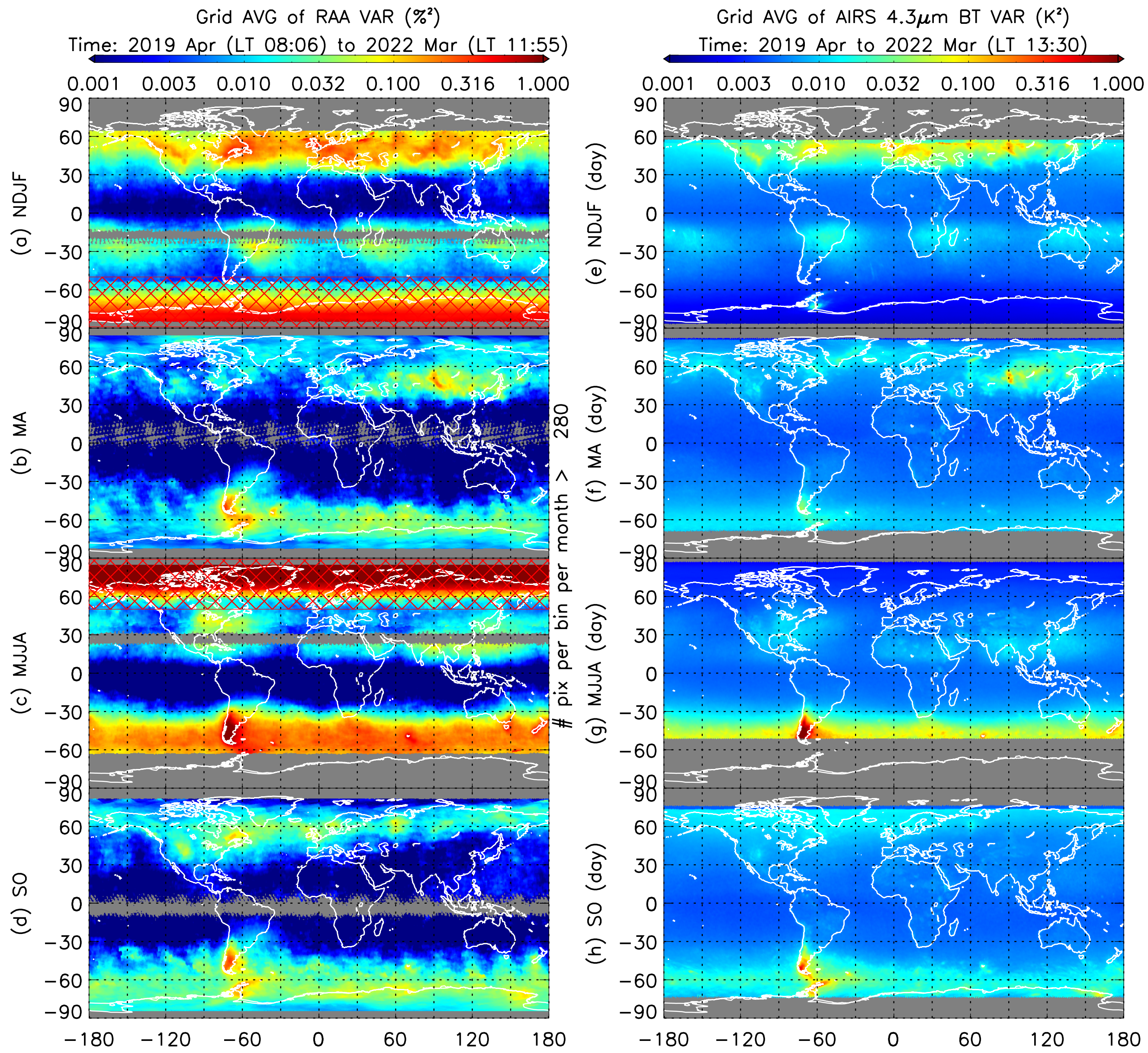

Figure 4. (a–d) Seasonally averaged Rayleigh Albedo Anomaly (RAA) variance distribution based on 3 years of RAA data obtained by cloud imaging and particle size (CIPS) from April 2019 to March 2022. The horizontal resolution of the longitude-latitude grid is 0.5° × 0.5°. Note that colorscale is logarithmic. The cross-hatched regions denote regions in which polar mesospheric clouds contaminate the RAA retrievals. Gray shading denotes regions with insufficient sampling, where grid points have less than 280 pixels per month (see caption of Figure S4 in Supporting Information S1 for further explanation). The maps combine data for (a) November–February representing boreal winter, (b) March and April representing boreal spring, (c) May–August, and (d) September and October. (e–h) Same as (a–d), but seasonal gravity wave variance distribution based on Atmospheric InfraRed Sounder (AIRS) 4.3 μm brightness temperature data. To match CIPS, only daytime AIRS pixels (pixels with solar zenith angle ≤76.5°) are included.

the westward wind is strong in the summer hemisphere, while in the winter hemisphere, the eastward wind has an even stronger magnitude (Lindzen, 1981). Due to the wind filtering effect, the stratospheric wind provides favorable conditions for upward propagating GWs to reach the mesosphere during solstice seasons (Alexander & Barnet, 2007).

Previous studies suggest that the polar night jet focuses GWs poleward from the Andes mountains into a stratospheric hotspot at 60°S (e.g., Hindley et al., 2015; Sato et al., 2009; Watanabe et al., 2008, etc.). In the report of Trinh et al. (2018), based on SABER observations in the altitude range of 30–75 km, the regions with high GW momentum fluxes in the summer hemisphere gradually move poleward and diminish. Those studies are consistent

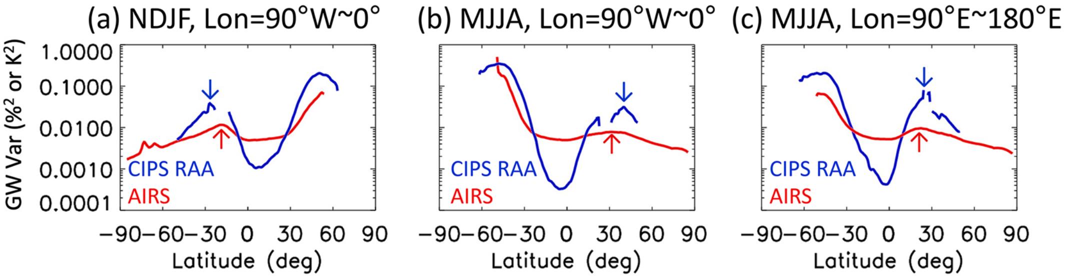

Figure 5. (a) Zonal averaged gravity wave (GW) variances within longitude range from 90°W to 0° derived from cloud imaging and particle size (CIPS) Rayleigh Albedo Anomaly (RAA) (blue) and Atmospheric InfraRed Sounder (AIRS) 4.3 μm brightness temperature data (red) in November to February (NDJF) season; (b) the same as (a) but in May–August (MJJA) season; (c) the same as (b) but within longitude range from 90°E to 180°E. The arrows represent the latitudes of local peaks of GW variances in CIPS (blue) and AIRS (red).

with the discussion in Forbes et al. (2021) that GWs generated from low latitude regions shift poleward as they ascend. Since the peak weighting function for AIRS 4.3 μm bands (30–40 km) and for CIPS RAA (50–55 km) are different (Figure 3), we can confirm a similar pattern by comparing the latitudes of hotspots observed by the two instruments. In Figure 5a, the blue and red curves show the zonally averaged GW variances in CIPS RAA and AIRS within the longitude range from 90°W to 0° during NDJF. The red and blue arrows represent the latitudes of local maxima in the variances of the Southern Brazil hotspot observed at altitudes 30–40 and 50–55 km, respectively. Similarly, the two arrows in Figure 5b represent the latitudes of the Northern American hotspot during MJJA, and the two arrows in Figure 5c represent the latitudes of the South Asia-Pacific hotspot during MJJA. The locations of the two arrows in each plot suggest a poleward shift of the GW hotspot from the stratosphere (red arrows) to the lower mesosphere (blue arrows), consistent with the previous work cited here. However, because of the missing CIPS data caused by satellite yaw maneuvers, and also possibly because the peak altitudes of the AIRS and CIPS weighting functions differ by only ∼15 km, we cannot make a more quantitative statement about this seemingly poleward shift tendency.

Figure 4 shows that both CIPS and AIRS indicate much weaker GW variances during equinox seasons (MA and SO). Unfortunately, as mentioned in Section 2.2 and Figure S4 in Supporting Information S1, CIPS has a relatively low sampling data rate due to the smaller width of the orbit strip. A consequence is that a 3-year data set of CIPS observations is still insufficient to achieve robust statistics during the 2-month equinox seasons, and artifacts (orbital signatures) appear in the results (e.g., striations at 50°S in Figures 4b and 4d). Nevertheless, there are still notable and meaningful differences between CIPS and AIRS. For example, CIPS shows a more significant GW variance belt than AIRS at ∼60°S in MA (Figure 4b vs. Figure 4f) and also at ∼60°N in SO (Figure 4d vs. Figure 4h).

To further investigate the month-by-month changes in GW variance with higher time resolution, we plot the monthly gridded mean GW variance obtained from CIPS (Figure 6) and AIRS (Figure 7), respectively. In general, we find excellent agreement in the CIPS and AIRS data sets for the distribution of major GW hotspots. Of particular interest are the transitions from March to April and from September to October. CIPS shows high variance in the Northern Hemisphere and low variance in the Southern Hemisphere in March, switching to high variances in the Southern Hemisphere and low variances in the Northern Hemisphere in April. The opposite transition is observed from September to October. We attribute these changes to two factors: on one hand, orographic and polar vortex-related GW activity in the winter hemisphere rapidly changes around the equinoxes, likely because the zonal wind changes sign, which prevents orographic GWs from reaching higher altitudes right before local autumn equinox or right after spring equinox. Polar vortex GWs depend on the strength of polar night jet. The polar night jet abruptly strengthens and weakens with the transition to winter and spring, respectively. In this scenario, both GW source and wind filtering effects play an important role in the presence of GWs in the middle atmosphere. On the other hand, the wind magnitudes around the equinoxes are small, which makes convectively generated GWs difficult to observe by nadir viewing instruments, because their vertical wavelengths are small (e.g., Forbes et al., 2021). Although convective activity in mid- and high-latitudes at equinox is not as strong as during the local summer season, convection still produces significant numbers of GWs, which can be observed by limb sounders such as SABER that can detect waves with shorter vertical wavelengths (e.g., subfigure March

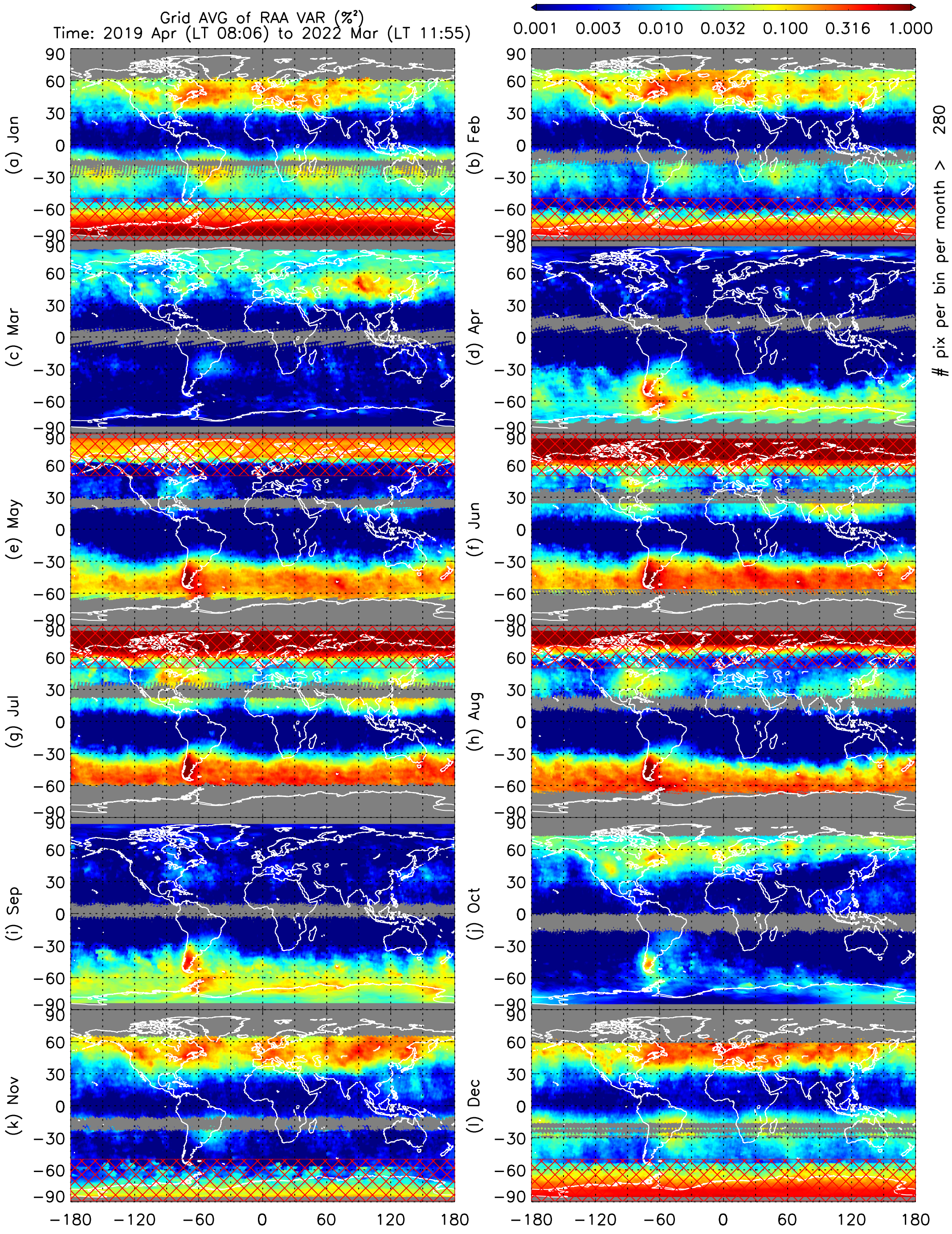

Figure 6. The monthly gravity wave variance distribution based on 3 years (April 2019 to March 2022) of cloud imaging and particle size Rayleigh Albedo Anomaly (RAA) data obtained. Cross-hatched regions denote regions in which Polar Mesospheric Clouds interfere with RAA retrievals.

in Figure 2 in X. Liu et al., 2019). In this scenario, the wind filtering effect plays a dominant role in the presence of GWs in the middle atmosphere. Section 4 discusses the possible causes of GW variance differences between the two data sets near equinox.

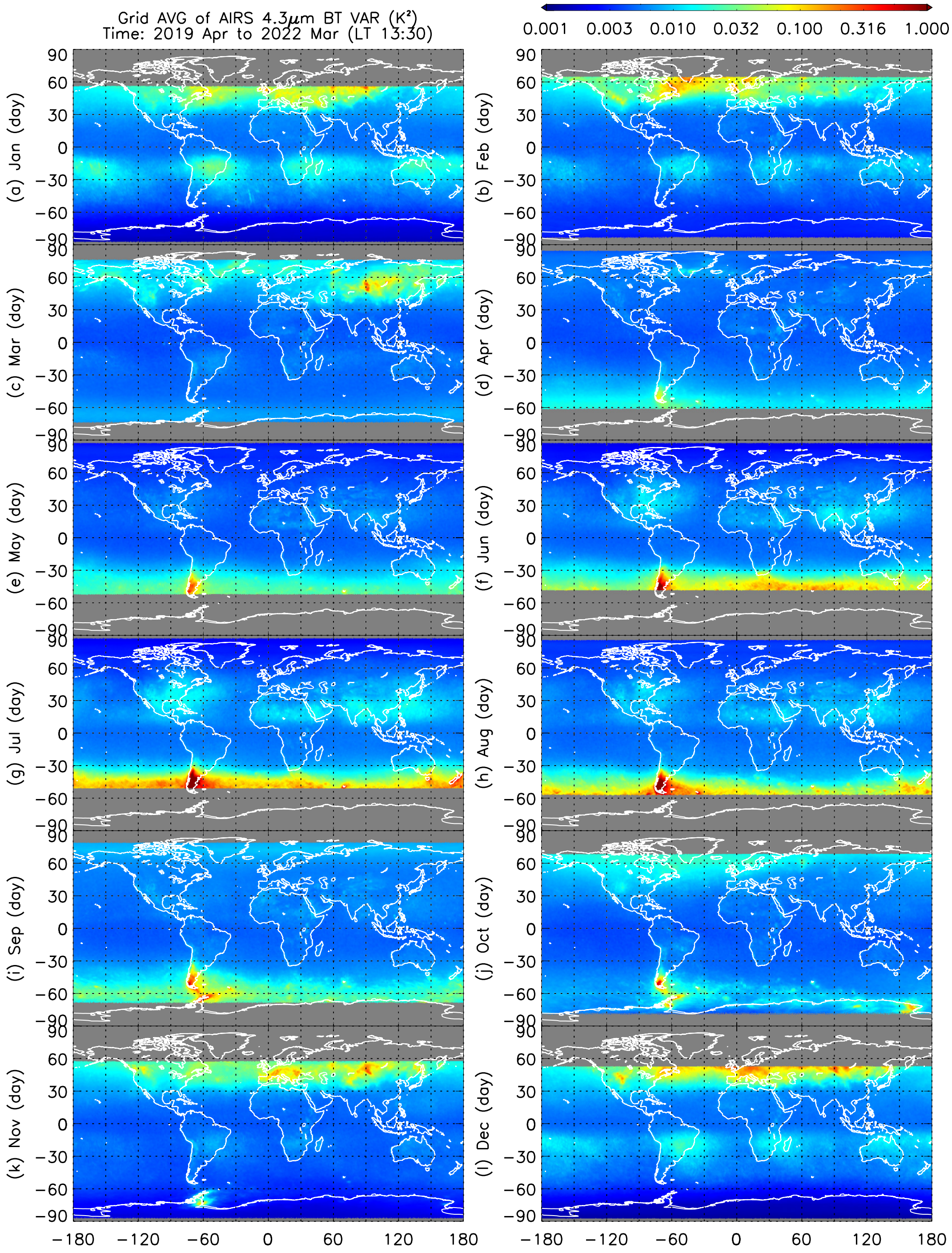

Figure 7. The monthly gravity wave variance distribution based on 3 years (April 2019 to March 2022) of Atmospheric InfraRed Sounder 4.3-μm brightness temperature (BT) perturbation data. Because 4.3-μm BTs observed in the absence of sunlight have higher variance due to typically higher nighttime noise (Hoffmann et al., 2014), pixels with the solar zenith angle >76.5° are not included here.

3.2. Seasonal GW Event Frequency in CIPS and AIRS

GWs often exhibit spatial and/or temporal intermittency in occurrence frequency, amplitude, and spectral properties (Kruse et al., 2023). This is a largely unconstrained GW parameter in numerical studies. To investigate GWs on a global scale for different atmospheric conditions, we follow Hoffmann et al. (2013) and define the "peak event frequency" as the ratio in each longitude by latitude grid cell of the number of measurements (pixels) that exceed a specified wave detection threshold to the total number of measurements. The term "peak event" means the detected strong GW events for which the local RAA variances (obtained by CIPS) or BT variances (obtained by AIRS) significantly exceed background levels. A location with a high PEF is often related to GW sources like orography and/or convection.

Following Hoffmann et al. (2013), the detection threshold in each grid cell is defined by

$$\sigma_T^2(\theta) = \overline{\sigma^2}(\theta) + n \times \sqrt{\frac{1}{N-1}\sum_{i=1}^{N}\left[\sigma^2(\theta_i) - \overline{\sigma^2}(\theta)\right]^2}, \tag{4}$$

where

$$\overline{\sigma^2}(\theta) = \frac{1}{N}\sum_{i=1}^{N}\sigma^2(\theta_i). \tag{5}$$

Here the term $\overline{\sigma^2}(\theta)$ is the average variance within each latitude band θ where ($\theta = 0°, \pm10°, \pm20°, \ldots, \pm90°$) and $\theta - 5° \le \theta_i < \theta + 5°$. The term with the square root sign in Equation 4 is the unbiased sample standard deviation of variances at latitude θ, N is the total number of variance values per latitude band and "n" is meant to give a number of how many standard deviations above the mean we consider a data point a "peak event," which can be adjusted to get optimal visual results. In Hoffmann et al. (2013), the factor $n = 5$, while in this study, we define $n = 3$. To determine thresholds $\sigma_T^2(\theta)$, Hoffmann et al. (2013) first collected all BT variance data from AIRS data located between 160°W and 180°W. This longitude sector is located in the central Pacific primarily over the ocean where convective activity is less frequent. In our study, for simplicity, we determine threshold $\sigma_T^2(\theta)$ values based on all observations with longitudes from 180°W to 180°E, and θ are latitude bins that are used to define the latitudes of map grids ($\theta = 0°, \pm0.5°, \pm1°, \ldots, \pm90°$) and $\theta - 0.25° \le \theta_i < \theta + 0.25°$. We follow the iterative approach in Hoffmann et al. (2013), whereby GW variances larger than the initial threshold $\sigma_T^2(\theta)$ are excluded from the data set, and the final variance thresholds are calculated by applying Equations 4 and 5 again. We conducted a sensitivity analysis involving the factor n and the width of latitude bins θ. Our findings indicate that utilizing parameters with these values yields results in line with previous studies and optimizes the comparability between CIPS and AIRS data for our intercomparison.

The final thresholds are derived month by month. Figure 8 shows the zonal averages of final detection thresholds for December, March, June, and September, for RAA variance (Figure 8a), and AIRS daytime 4.3 μm BT variance (Figure 8b). The AIRS final thresholds in Figure 8b (April 2019 to March 2022) and the AIRS final thresholds (2003–2008) derived and published by Hoffmann et al. (2013, in their Figure 5) are in agreement (not shown). Hoffmann et al. (2013) pointed out that changes in the thresholds in the equatorial region throughout the year are relatively small. Compared to AIRS final thresholds in Figure 8b, Figure 8a shows comparable RAA final thresholds at high latitudes in solstice seasons. However, RAA final thresholds are higher than for AIRS at sub-solar latitudes (i.e., 10°–30°N for June and 10°–30°S for December), which are the latitudinal ranges that include GW hotspots generated by summertime convection. The discrepancies between CIPS and AIRS at low latitudes around solstices can be explained by two reasons: (a) convection-generated GW activity tends to have relatively smaller-scale GWs, and CIPS data is more sensitive to them due to higher resolution. (b) Zonal wind magnitudes are generally higher at the stratopause than in the stratosphere, so the wind filtering effect provides more favorable conditions for the upward propagating GWs to be observed by CIPS. Meanwhile, RAA final thresholds are lower at minima near the equator, which corresponds to latitude bands in which the zonal wind magnitude is close to zero and GW activity is less compared to other latitude ranges. Because of higher SNR, there is less noise-induced variance in the CIPS RAA data set. During equinox seasons, RAA final thresholds and AIRS final thresholds show similar variations.

Figures 8c and 8d show how the final thresholds at different latitudes evolve over the course of the year. Both CIPS and AIRS observed a rapid interhemispheric change around equinoxes. Figures 8e and 8f show the meridional averaged GW variance from 30°S to 30°N, in which there are six peaks in total, three for MJJA season at around 50°W–100°W, 20°W–60°E, 70°E−160°W, and three for NDJF season at around 30°W–70°W, 20°E−80°E, 120°E−160°W. According to Forbes et al. (2022), these six peaks are originated from six monsoon regions, respectively: Central America, North Africa, the South Asia-Pacific region, South America, South Africa, and the Malay Archipelago/Australia-Pacific region. Figures 8c–8f are in agreement with Figures 2 and

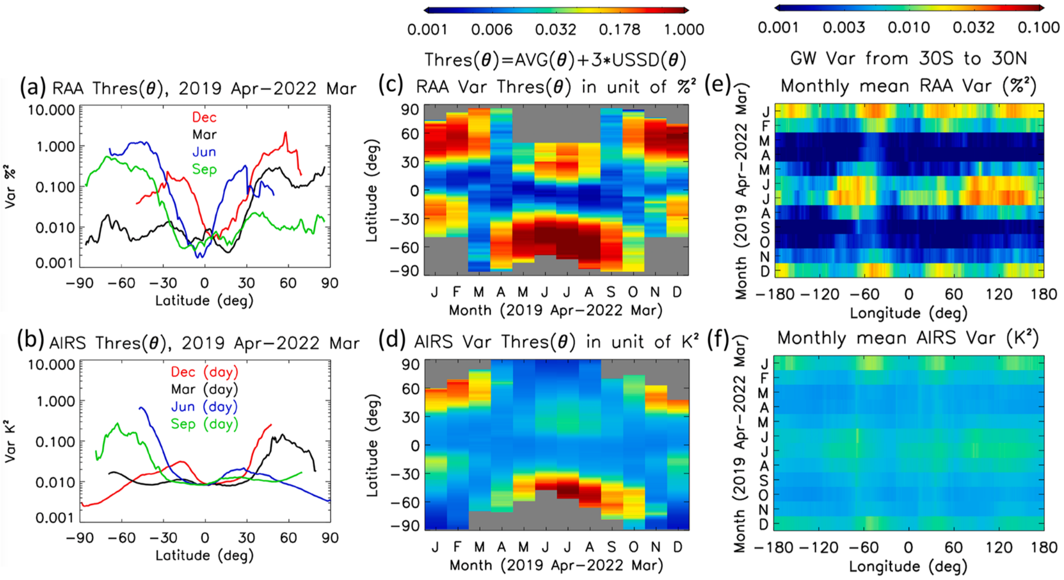

Figure 8. (a) The maxima of 3-year zonal-averaged final Rayleigh Albedo Anomaly (RAA) variance thresholds that are used in this study to detect GW peak events. For clarity, only the monthly maxima of December (red), March (black), June (blue) and September (green) during April 2019 to March 2022 are plotted. The RAA variances in the polar region during Polar Mesospheric Clouds (PMC) seasons (i.e., 50°S–90°S for December and 50°N–90°N for June) are omitted because they are contaminated by PMC scattering; (b) same as (a) but for Atmospheric InfraRed Sounder 4.3 μm brightness temperature (BT) variance (daytime). The BT variances observed during polar nights are systematically higher due to less non-local thermodynamic equilibrium effect (Hoffmann et al., 2014), so data derived from pixels with solar zenith angle >76.5° are not shown. (c and d) Same data as in (a, b) but displayed as a monthly time series versus latitude. (e) Longitude versus 3-year monthly average distribution of cloud imaging and particle size RAA gravity wave variance averaged over 30°S–30°N latitudes. (f) Same as (e) but of AIRS 4.3 μm BT variance.

3 in H. X. Liu et al. (2017), the latter of which shows the thermospheric GW hotspot distribution observed by Gravity Field and Steady-State Ocean Circulation Explorer satellite at altitudes of 220–280 km. This suggests stratosphere-thermosphere coupling via GWs.

Following the method used by Hoffmann et al. (2013), we first calculate the monthly PEFs of GW peak events by applying the detection algorithm described above, then we average the monthly PEFs within the same season from multiple years, giving each month the same weight. Figure 9 shows the seasonal PEFs based on CIPS RAA (left column, a–d) and AIRS 4.3 μm BT perturbations (right column, e–h) from April 2019 to March 2022. In Figures 9b and 9d, noise-like artifacts at low latitudes are caused by insufficient CIPS data due to the dayside yaw maneuver that is performed on each AIM orbit. The AIRS PEFs shown in Figures 9e–9h are almost identical to the AIRS PEFs in Hoffmann et al. (2013, Figure 6). Generally, the hotspots found in AIRS are also found in CIPS, for example, both AIRS and CIPS see the convective GW hotspots over the east US in boreal summer (Hoffmann & Alexander, 2010). As a further description, Section 4 discusses the major hotspots seen by both instruments, but it is important to note that there is not necessarily a one-to-one correspondence between the seasonally averaged GW variances (e.g., Figure 4) and the PEFs (Figure 9). Notable differences between CIPS and AIRS PEFs include: (a) CIPS sees a persistent hotspot over Southern Brazil that is much weaker or absent in AIRS, (b) CIPS sees a stronger and more persistent GW hotspot in the region of the Indochina Peninsula and Maritime Continent than what is seen by AIRS, (c) AIRS sees an enhancement of high PEF over central Africa in boreal spring and summer that is not observed by CIPS, and (d) AIRS sees a weak but well-defined hotspot stretching from Utah to Mexico year-round that is not as evident in CIPS in March–August. These four major differences are denoted by red rectangles marked with corresponding numbers in Figure 9.

As discussed more in Section 4.1, differences in seasonal PEF hotspots due to convective GWs, such as mentioned above in Equations 1 and 2, might be due to the diurnal cycle of convection and AIRS and CIPS measuring at different local times (Forbes et al., 2021). The seasonal PEF hotspots that are seen by AIRS but not CIPS, as mentioned above in Equations 3 and 4 and elsewhere, occur at the boundaries between the deserts and water (lakes, rivers or seas) in low latitudes under sunlit conditions. During daytime, the AIRS 4.3 μm BT

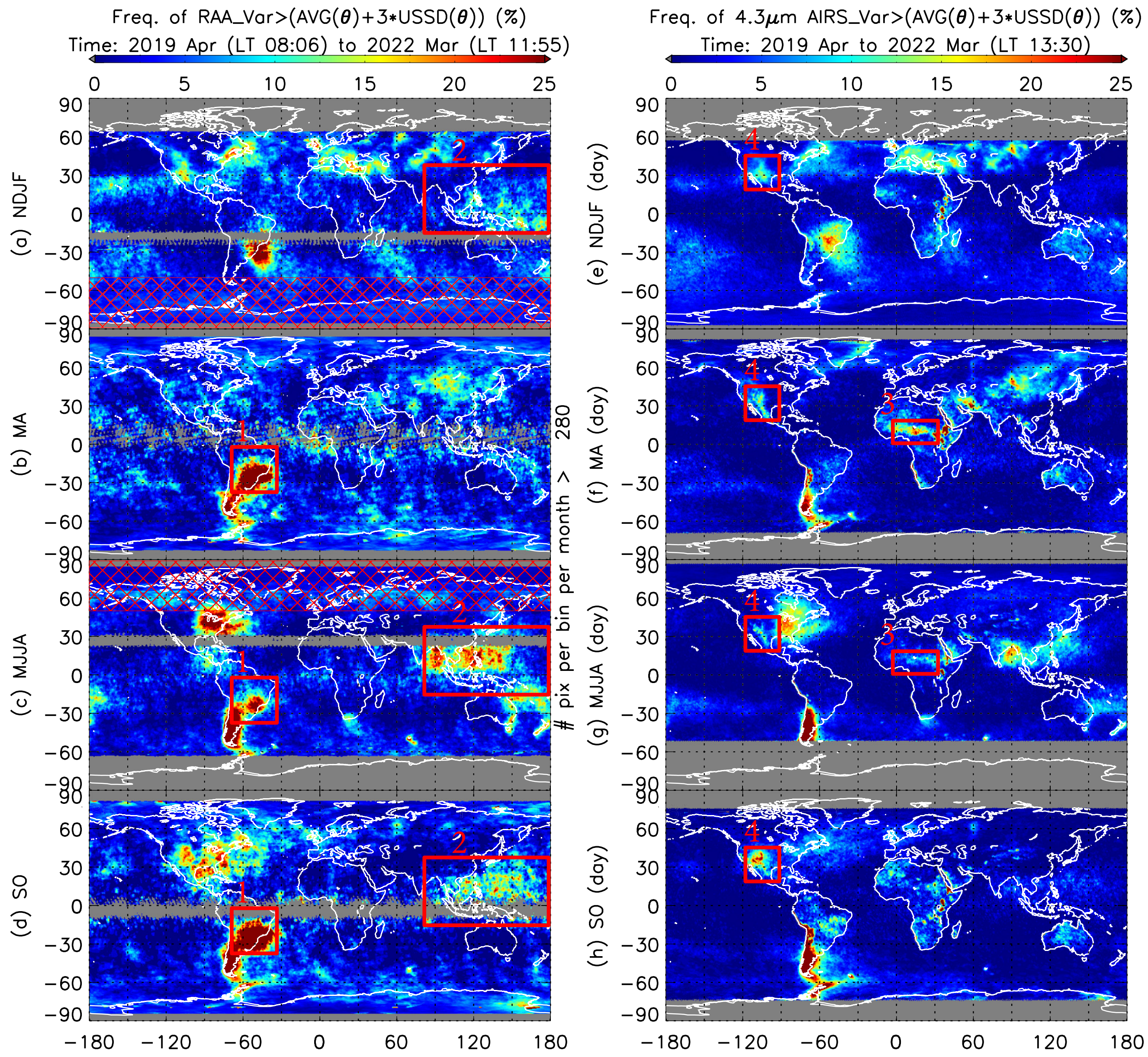

Figure 9. (a–d) Seasonal peak event frequencies (PEFs) derived from Rayleigh Albedo Anomaly (RAA) variance based on 3 years of RAA data obtained by cloud imaging and particle size (CIPS) from April 2019 to March 2022. (e–h) Seasonal PEFs derived from Atmospheric InfraRed Sounder (AIRS) 4.3 μm brightness temperature perturbation variance based on 3 years of AIRS data (daytime) from April 2019 to March 2022. The red boxes denote four regions that show differences between CIPS and AIRS PEFs: (1) Southern Brazil, (2) Maritime Continents, (3) central Africa, (4) Utah–Mexico region.

is usually lower at the water side than at the desert side near a water-desert boundary in low latitudes. Hoffmann et al. (2014) explain that these PEF hotspots are due to very large surface temperature contrasts between desert and water (up to 40 K), which results in small biases (0.1 K) in 4.3 μm BT and significant BT variances over water-desert boundaries. Therefore, caution is advised when analyzing those high variances in AIRS data as they are not caused by real atmospheric waves.

4. Significant GW Hotspots Observed by CIPS and AIRS

4.1. Comparison of GWs Over Southern Brazil and Southern Andes

Here, we focus on CIPS and AIRS observations over southern Brazil and over the nearby Southern Andes region. There is a significant difference between the PEFs derived from CIPS and from AIRS over southern

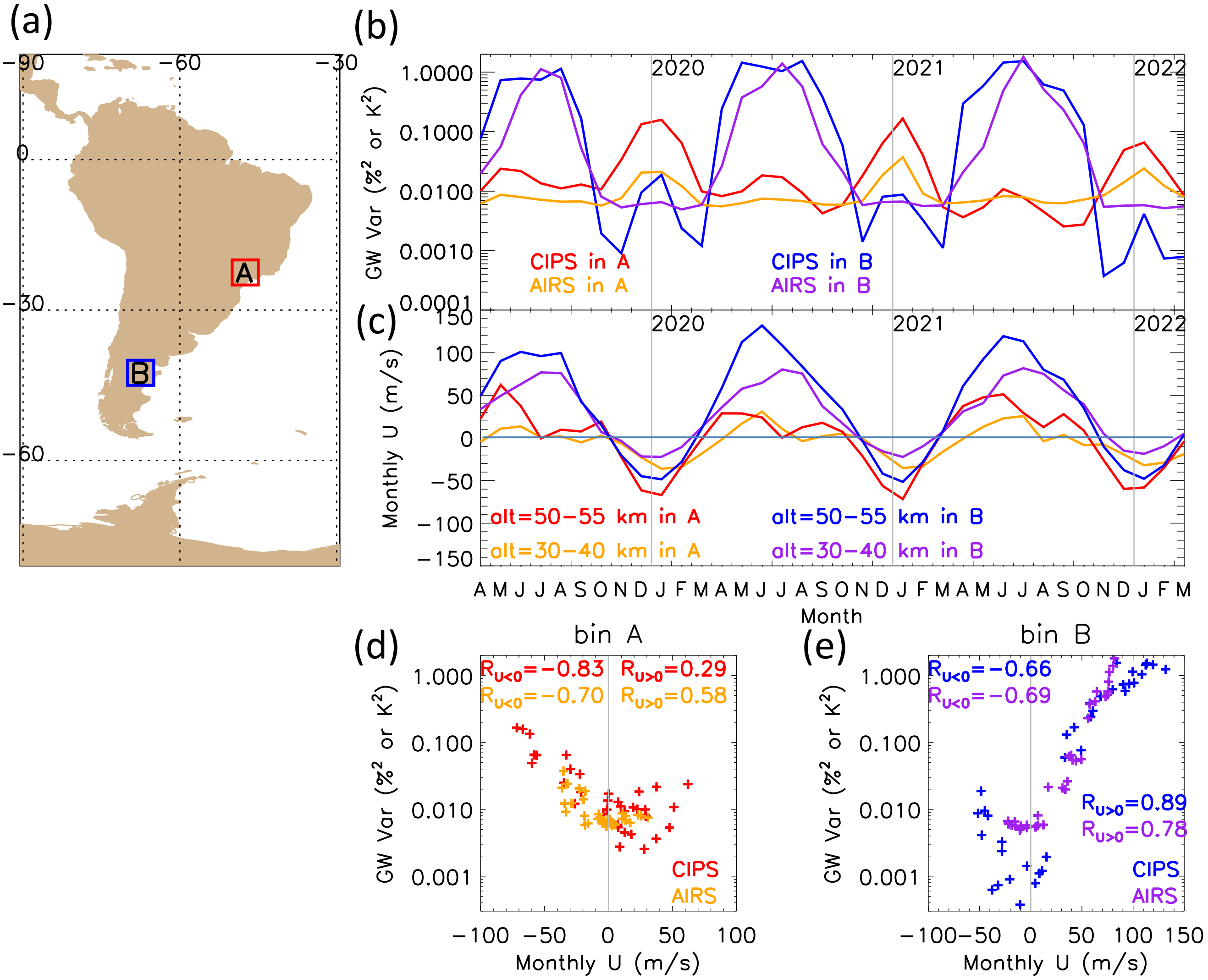

Figure 10. (a) Map showing the two 5° × 5° square bins marked "A" and "B" along the southeast coast of South America; bin A is located at the center of southern Brazil region, bin B is located inside the southern Andes region. (b) Time series of monthly mean cloud imaging and particle size (CIPS) Rayleigh Albedo Anomaly (RAA) variance and daytime Atmospheric InfraRed Sounder (AIRS) 4.3 μm brightness temperature perturbation variance over bin A (orange: AIRS, red: CIPS) and bin B (purple: AIRS, blue: CIPS) denoted in the map in panel (a). (c) Time series of monthly Modern-Era Retrospective Analysis for Research and Applications, Version 2 stratospheric zonal wind at altitude 30–40 and 50–55 km over bin A (orange: 30–40 km, red: 50–55 km) and bin B (purple: 30–40 km, blue: 50–55 km) at UT 12–18 hr (LST ~8–14 hr). In panel (b, c), each tick on the horizontal axis denotes the first day of a month, and gray vertical lines denote 1 January. (d) Scatter plot of gravity wave (GW) variances relative to in situ zonal winds over bin A and Pearson correlation coefficient R of zonal wind ($U > 0$ and $U < 0$ separately) versus GW variances (orange: AIRS, red: CIPS). Panel (e) same as panel (d) but over bin B.

Brazil (Figure 9). Forbes et al. (2021) studied the southern Brazil hotspot using CIPS RAA data acquired during the Southern Hemisphere monsoon season (December–February). They pointed out that, according to Sato et al. (2009), those GWs propagate upward and southward toward the westward jet core in the middle atmosphere, and the convective source over the Brazilian rainforest region is the cause of this hotspot. Figure 9 (left column) shows that CIPS observations indicate that the hotspot over southern Brazil is present not only during the Southern Hemisphere monsoon season, but also outside the monsoon season. That is, CIPS captured a significant PEF hotspot over the southern Brazil region in all seasons, signifying that GW events over southern Brazil are persistently higher (both in amplitude and frequency) than at other longitudes near a latitude of ~25°S throughout the year. However, AIRS did not observe this hotspot during non-monsoon seasons, as shown in the right column of Figure 9. This discrepancy is investigated in Figure 10.

Figure 10 shows the time series of monthly mean GW variances of CIPS RAA and AIRS 4.3 μm BT perturbation over two 5° × 5° square bins in the southern Brazil region and southern Andes region, respectively, in panel (a).

Figure 10b indicates that GW variances for both instruments maximize in austral summer over southern Brazil (bin A; red for CIPS, orange for AIRS), and in austral winter over the southern Andes (bin B; blue for CIPS, purple for AIRS). However, as alluded to above in the discussion of Figure 9, the austral summertime (NDJF) GW variance maximum observed by CIPS over southern Brazil (bin A) is about 4–10 times larger than that observed by AIRS (note the log scale). In addition, CIPS observes a GW variance peak in austral summer over the southern Andes (bin B) that is not observed by AIRS. To aid in the interpretation of Figure 10b, time series of MERRA-2 monthly mean zonal winds averaged over altitudes corresponding to the CIPS and AIRS GW observations are plotted in Figure 10c for bin A (red for CIPS altitude range, orange for AIRS altitude range) and bin B (blue for CIPS altitude range, purple for AIRS altitude range). In addition, Figures 10d and 10e show scatter plots of monthly GW variances versus zonal wind velocity for observations in bins A and B. As shown by Figures 10c–10e, GW variances and monthly zonal wind magnitudes are generally strongly correlated, with absolute correlation coefficient $|R| \sim 0.6$–0.9 (except for CIPS in bin A when $U > 0$, which has $R \sim 0.3$). In both bins the prevailing winds are eastward (positive) in local winter and westward (negative) in local summer. As explained next, the summertime differences between CIPS and AIRS GW measurements can be attributed to effects of these winds on the observations.

The wind-GW relationship can be explained by the GW dispersion relation (Fritts & Alexander, 2003):

$$\omega_I^2 = \frac{N^2 k_H^2 + f^2\left(m^2 + \frac{1}{4H^2}\right)}{k_H^2 + m^2 + \frac{1}{4H^2}}. \tag{6}$$

In Equation 6, $\omega_I = 2\pi/\tau_I$ is the intrinsic frequency (τ_I is the intrinsic wave period), N is the buoyancy frequency, H is the scale height. $k_H = 2\pi/\lambda_H$ and $m = 2\pi/\lambda_z$ are the horizontal wavenumber and vertical wavenumber. f is the Coriolis parameter. According to Forbes et al. (2021), GWs with $\lambda_H < 400$ km should have a frequency much higher than the Coriolis parameter f. Hence, it is reasonable to assume that the GWs studied here are non-inertial, as the effect of the Coriolis force is negligible, and the dispersion relation simplifies to

$$m^2 = \frac{N^2}{c_I^2} - \frac{1}{4H^2} - k_{\mathrm{H}}^2. \tag{7}$$

This equation is equivalent to Equation 1 in Forbes et al. (2021) and Equation 6 in Vadas (2007), and shows the anelastic GW dispersion relation for medium- and high-frequency GWs. In Equation 7, $c_I = \frac{\lambda_H}{\tau_I} = \frac{\lambda_H}{\tau} - U$ is the intrinsic phase speed (U is the zonal wind and τ is the ground-based wave period). For waves with $\lambda_z \gtrsim 30$ km, the $1/4H^2$ term (i.e., compressibility term) should be retained since $H \approx 7$ km in the middle atmosphere (Fritts & Alexander, 2003). Using a spectrum of convectively generated GWs based on Equation 7, Forbes et al. (2021) proved that increasing westward wind would increase λ_H and λ_z and potentially moves an eastward-traveling wave into the CIPS observational filter via Doppler shifting (the same rule applies to AIRS, although AIRS has a lower horizontal resolution). For example, with a stratospheric value of $N = 0.02\ \mathrm{s}^{-1}$ and $H = 7$ km, when westward wind increases by 30 m/s (e.g., from $U = 0$ to $U = -30$ m/s), a wave with wavelengths of $(\lambda_z, \lambda_H) = (10, 28)$ km (CIPS cannot observe) can be shifted to a wave with $(\lambda_z, \lambda_H) = (21, 55)$ km (CIPS is able to observe) (Forbes et al., 2021). For mountain waves, since ground-based phase speed is close to 0, the c_I^2 term in Equation 7 can be replaced by U^2. As the background wind gets larger at higher altitude, $|m|$ gets small and λ_z gets large. The conclusion to be drawn is that during non-equinox seasons, the stronger background winds in higher altitudes can lengthen the λ_z of upward propagating GWs, leading to a more preferable condition for GWs to be observed by CIPS than by AIRS.

In Figure 6, the monthly RAA results show that the Southern Andes region has strong GW variance peaks during local winters (April–October). In contrast, the topography of southern Brazil is less conducive to GW generation. On the other hand, GW activity over southern Brazil is observed by CIPS throughout the year, which is why Figures 9a–9d show a PEF hotspot over southern Brazil in all seasons. Regions within bins A and B are under the influence of both the southern Brazil and southern Andes hotspots. These influences are detectable if the instrument is sensitive enough. For example, the CIPS RAA GW variances of bin A (red curve in Figure 10b) have peaks during April and October, which are caused by orographic GWs originating from the Southern Andes hotspot. Unfortunately, in seasonal results, RAA variances are averaged out by other months in the same group, so “equinox minima” are hardly seen in Southern Brazil in Figures 4b and 4d. Nevertheless, “equinox minima” over Southern Brazil can be recognized in monthly results in Figure 6. In the same way, CIPS RAA GW variances in bin B have minor peaks in local summers between March and November, which are also more easily recognized in Figure 6 than in Figures 4a–4d. Although CIPS RAA minor peaks are apparent with the log scale used in Figure 10b, these RAA minor peaks with an order of magnitude of about 0.01 are not apparent in Figure 4 because the magnitudes of those peaks are so small that they can be easily averaged out by multiple months of data. As shown in Figure 10c, the monthly zonal wind magnitudes in equinox seasons are ~0 m/s for both altitude ranges of 30–40 and 50–55 km, but the "equinox minima" pattern for GW activity is only shown in GW variances obtained from the CIPS RAA data set. This suggests a lower background noise in the CIPS RAA signal, and thus a higher SNR for detecting small-scale GWs compared to AIRS. It is worth mentioning that in Figure 9a, the PEF hotspot over southern Brazil is shifted toward the ocean, which is a typical signature for convective GWs as easterly wind shifts the peak toward east. Compared to convective GWs, topographic GWs in the other three seasons are more vertical and confined to the local.

When analyzing convective GWs observed in CIPS and AIRS, it is important to consider the impact of different local times at which satellite measurements are taken. The variations in convective GW hotspot patterns between the two data sets can largely be attributed to the diurnal cycle of convection, where convective sources at different local times exhibit varying strengths. For instance, Forbes et al. (2021) found that higher rainfall rates during CIPS measurements correspond to larger observed GW variances in CIPS. It is possible that CIPS measurements were captured closer to the peak of local daily convective activity, whereas AIRS measurements were not. Additionally, the propagation time of GWs should be considered. Depending on the spectral characteristics of the convective waves (Hoffmann & Alexander, 2010), it can take anywhere from tens of minutes to several hours for GWs to propagate from tropospheric convective sources to the mid-stratosphere (AIRS), and even significantly longer to reach the stratopause/lower mesosphere (CIPS). As a result, the local time difference in convective activities generating GWs observed in CIPS and AIRS is generally larger than the local time difference between the measurements of the two instruments.

4.2. GWs Over Islands in the Southern Ocean

In the climatological study of Hoffmann et al. (2013), the small mountainous islands in the Southern Ocean are categorized as GW hotspots from May to September. Alexander and Grimsdell (2013) discussed stratospheric perturbations caused by islands in the Southern Ocean based on AIRS 15 μm BT observations. Their study showed that seasonal variations of those GWs closely relate to latitude and prevailing wind patterns. These articles suggested that stratospheric winds have a first-order limiting effect on the occurrence frequencies of those GWs in satellite observations, while surface wind direction and island orographic relief exert a secondary influence. Alexander and Grimsdell (2013) estimated the momentum flux of GWs generated by flow over islands and their importance to the general circulation of the Southern Hemisphere. Their estimation, based on AIRS observations, suggests that the cumulative effects of these GWs may be a substantial fraction of the "missing flux" in climate models in the Southern Hemisphere stratosphere. Owing to high horizontal resolution, CIPS is well-suited to observe these small-scale island waves (e.g., mountain waves over the Kerguelen Islands, Randall et al., 2017). In our study, the effects of island GWs are prominent in the CIPS and AIRS seasonal results. For example, Figures 4 and 9 and Figure S1 in Supporting Information S1 have clear Southern Ocean island wave signatures within the latitude belt from 30°S to 60°S.

Analogous to Figure 10, Figure 11 shows the time series of monthly mean GW variances of CIPS RAA and AIRS 4.3 μm BT perturbation at several locations in the Southern Ocean. For simplicity, only three 2° × 2° bins are analyzed, including two bins with islands (bin P with PEI or Prince Edward islands, and bin K with Kerguelen islands) and one bin without any island (bin N with no island). As shown in Figure 11b, the temporal variations of the GW variances in all three bins are similar to the temporal variations shown in Figure 10b for the Southern Andes. For example, GW variances of both CIPS and AIRS have maxima in austral winters; and CIPS GW variances have peaks in austral summers, but AIRS variances do not show these peaks. Because the latitudes of the three bins in Figure 11a and bin B in Figure 10a are close, their similarity in GW variance pattern over time can be explained by the same reason: during austral winters, strong polar vortices produce significant GWs, forming winter peaks in GW variances; in the austral summers, due to the southward propagation of convection-generated GWs from low-latitudes (i.e., three hotspots at Southern Brazil, Southern Africa, Malay Archipelago/Australia-Pacific region), GW variances in mid-latitudes also have related small peaks during

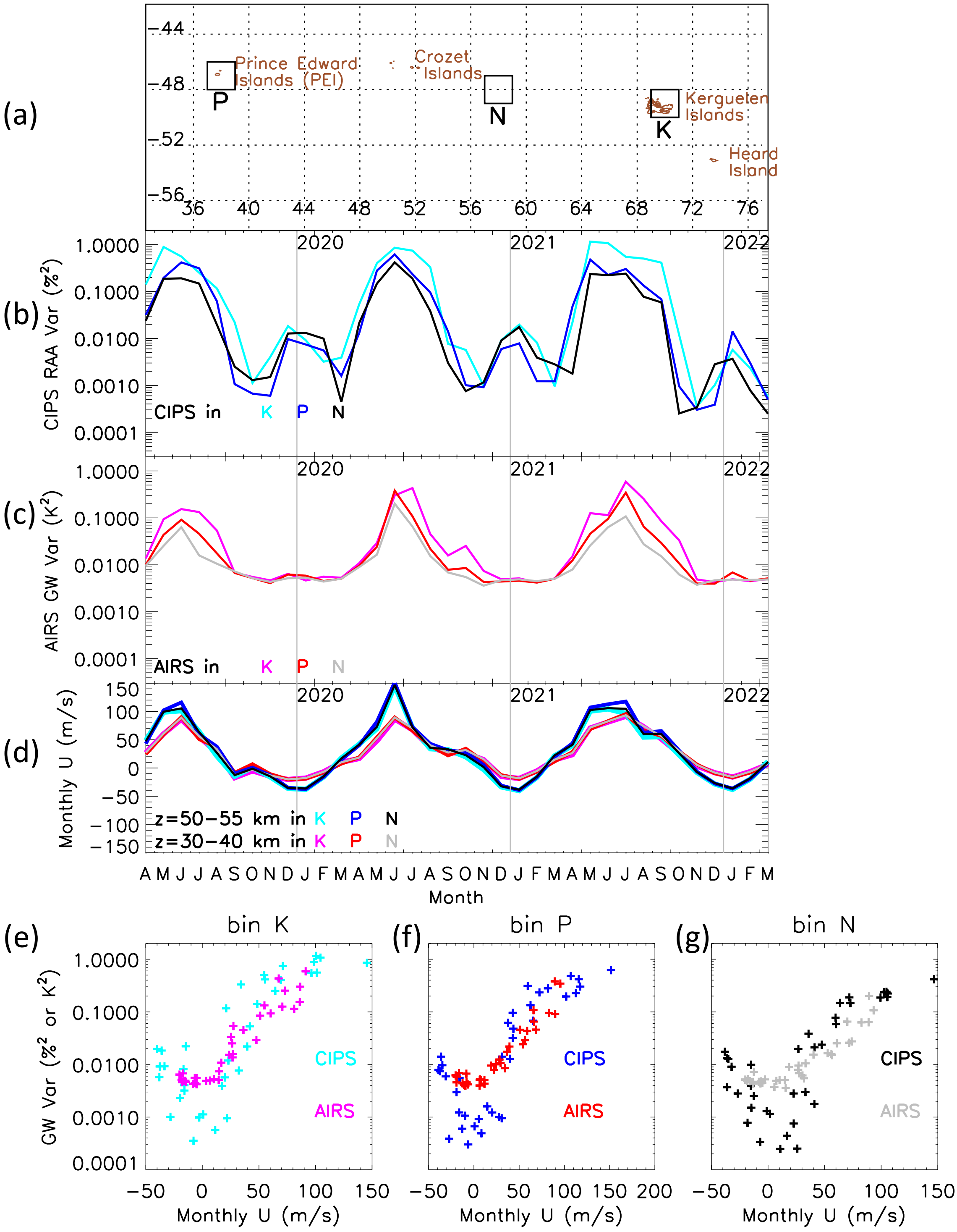

Figure 11. (a) Map showing the three 2° × 2° bins marked with "P" (includes Prince Edward islands), "K" (bin includes Kerguelen islands) and "N" (bin with no island) in the Southern Ocean. (b) Time series of monthly mean cloud imaging and particle size Rayleigh Albedo Anomaly variance over bin K (cyan), bin P (blue), bin N (black). (c) Time series of monthly mean daytime Atmospheric InfraRed Sounder 4.3 μm brightness temperature perturbation variance over bin K (magenta), bin P (red) bin N (gray). (d) Time series of monthly Modern-Era Retrospective Analysis for Research and Applications, Version 2 zonal wind at altitude 30–40 and 50–55 km over bins K, P, and N at UT 6–12 hr (LST ~8–16 hr for bins P, N, and K). In panels (b–d), each tick on the horizontal axis denotes the first day of a month and gray vertical lines denote 1 January. (e) Scatter plot of gravity wave variances relative to in situ zonal winds at altitude 50–55 km over bin K. Panels (f–g) same as panel (e) but over bin P and bin N, respectively.

summers. However, those wave signals in AIRS observations are obscured by noise due to the relatively low SNR of AIRS measurements, so AIRS does not show the small summertime peaks.

By combining GW variances and stratospheric zonal wind in scatter plots in Figures 11e−11g, we find that the GW-wind correlations of bins P, K, and N are very similar to Figure 10e, the Southern Andes scatter plot. The observations presented in Figures 11e−11g also follow the laws summarized by Alexander and Grimsdell (2013); that is, the stratospheric zonal wind is the first-order limiting effect on observed GW variances. For example, during winter seasons, the magnitudes of zonal wind speed and GW variances are highly correlated. Hoffmann et al. (2016) also found largest correlation of GW activity with zonal winds at ∼40 km of altitude. Among the three bins, the GW variance in bin K (includes the biggest islands in the map) is generally the highest, while in bin N (includes no island) is generally the lowest, which shows that surface conditions exert a secondary influence on stratospheric GWs. The results also indicate that a large proportion of GW variance originates from polar vortices. Exploring the relative contributions of orographic GW interaction with the jet stream and the in situ generation of GWs within the jet stream is an important direction for future research.

In the case study of orographic waves near the Kerguelen Islands and Heard Island, Hoffmann et al. (2014) compared AIRS 4.3 μm observations to IASI, and found higher variances in IASI, partly due to the better horizontal resolution of IASI. They explained that IASI has a smaller footprint size, which makes the instrument more sensitive to large amplitudes from short-scale waves. In the same way, CIPS has a higher horizontal resolution (56.25 km^2) than AIRS 4.3 μm BT perturbation (182.25–877.4 km^2). This highlights the importance of the CIPS RAA data set, because CIPS can resolve island GWs with smaller scales that AIRS cannot observe.

4.3. GWs Over Tropical Africa

Figure 12 shows the CIPS and AIRS GW variances over the tropical region of Africa during MA and MJJA. Note that the color scales in panels (a, b) are different than in Figure 4. Also note that in order to present a complete picture, Figure 12 includes the regions that are shaded in gray in Figures 4b and 4c, which indicate data of lower statistical significance. Fewer CIPS measurements are available at tropical latitudes because the AIM satellite performs a yaw maneuver at the subsolar latitude each orbit, during which observations are compromised. Nevertheless, Figure 12 presents clear evidence of GWs over Africa in MA and MJJA in both CIPS and AIRS data. Blanc et al. (2014) conducted a GW climatology study based on 10 years of observations at the IS17 infrasound station (Ivory Coast 6.67°N, 4.85°W) in the Inter-Tropical Convergence Zone (ITCZ). Based on data derived from microbarometers, they suggested that tropospheric GW activity was strong year-round and maximized in April and October. Although in the current study we do not observe year-round GW activity in the stratosphere over the same region, the CIPS GW PEFs are higher in equinox seasons than in solstice seasons over tropical West Africa (left column of Figure 9), partly consistent with the seasonal variation of tropospheric GW activity analyzed by Blanc et al. (2014).

Figures 12a and 12b clearly show that a GW hotspot over (or off the coast of) tropical West Africa occurs around equinox time. Of all the GW hotspots observed by CIPS and AIRS, this is the only GW hotspot that is centered over the Equator. The daytime AIRS observations are not shown here because of artifacts from the water-desert contrast, which was discussed in Section 3. The tropical West Africa GW hotspot occurs south of the ITCZ during the MA season. Blanc et al. (2014) explained the hotspot's location, suggesting that thunderclouds form in the monsoon flow due to the presence of the Gulf of Guinea and Congo basins. Based on an analysis of the seasonal variation in the location of the thunderstorms and GWs, they concluded that these thunderstorms were the source of the GWs observed over tropical West Africa.

As shown in Figures 12c and 12d, a notable GW hotspot extending across north Africa from the Sahara Desert to the Arabian Peninsula during MJJA is observed by both CIPS and AIRS. This hotspot was also discussed by Forbes et al. (2022), who studied the relationship between Outgoing Longwave Radiation (OLR) sources and GW momentum flux (derived from SABER) from 30 to 90 km in the Global Monsoon Convective System. Their results showed that there is a relationship between the OLR source over tropical West Africa and the North African GW hotspot during JJA. The elevated GW variances over northern Africa in MJJA shown in Figures 12c and 12d from both CIPS and AIRS are consistent with the conclusions in Forbes et al. (2022).

Taken together, the results in Figures 12a–12d present an interesting conundrum, if one assumes that the GWs marked in the four red circles in Figure 12 all originate from convective sources in tropical West Africa, as

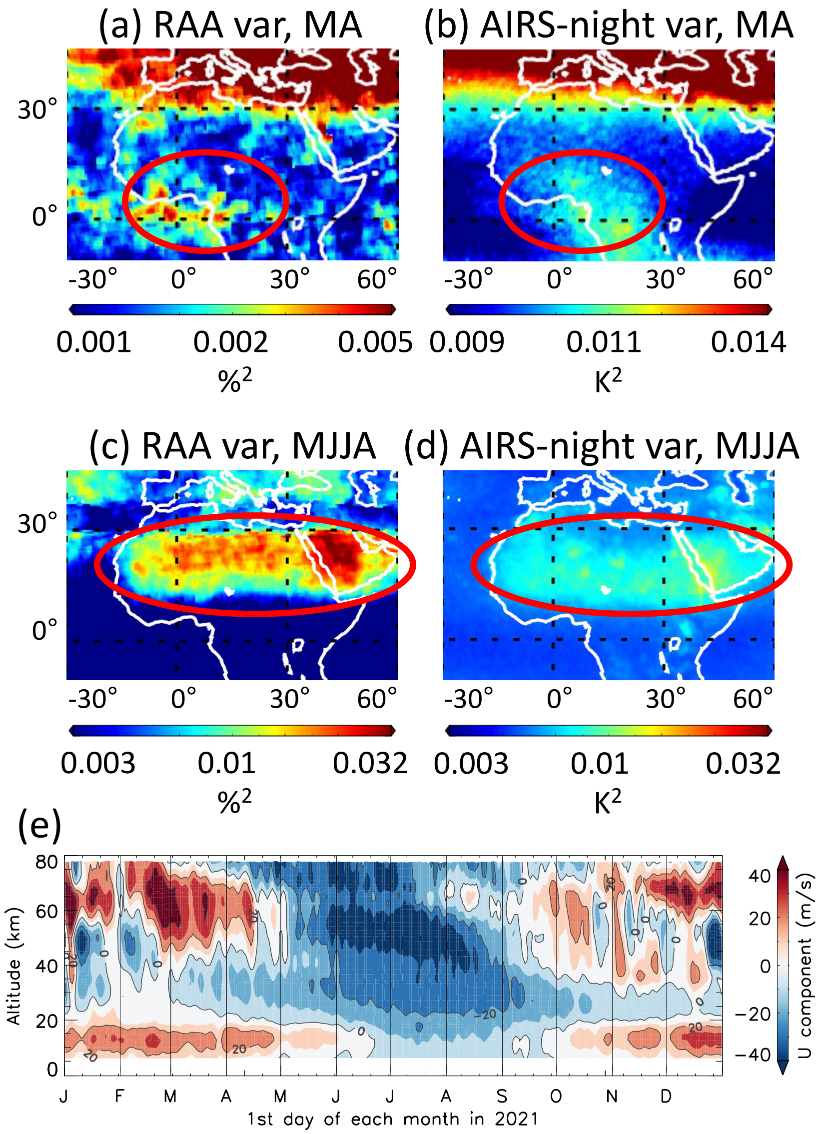

Figure 12. Gravity wave (GW) variances during March and April of 3 years (April 2019 to March 2022) based on (a) cloud imaging and particle size (CIPS) Rayleigh Albedo Anomaly (without grid filtering by the number of pixels) and (b) Atmospheric InfraRed Sounder (AIRS) 4.3 μm brightness temperature perturbation (nighttime) over Africa; (c, d) are the same as (a, b) but during May–August. Note that the color bar ranges in (a, b) are customized to highlight the tropical GW hotspot. The red circles signify the regions over Africa with relatively high GW variances that are the interest of discussion in this section. (e) Daily Modern-Era Retrospective Analysis for Research and Applications, Version 2 zonal wind profile in 2021 over the geographic region from 10° to 30°E and 10° to 30°N. The 12 and 18 UT output times are averaged on each day because their corresponding local times are close to the local times when CIPS and AIRS pass over.

might be inferred from the Blanc et al. (2014) and Forbes et al. (2022). The spring equinox results in Figures 12a and 12b (and in Figure S3b in Supporting Information S1) indicate elevated GW activity near the coast (CIPS) or inland (AIRS) of tropical West Africa, and the wintertime results in Figures 12c and 12d indicate elevated GW activity across northern Africa. What then determines the location change of the GWs observed by CIPS and AIRS in the different seasons? The deterministic factors may be the monthly variation of zonal wind in the middle atmosphere, as well as the seasonal changes of convective activity over Africa. A hypothesis to answer the question is: the presence of a westward jet and negative meridional wind gradient during the boreal summer season (MJJA) may pull the rising GWs poleward (Sato et al., 2009) and induce relatively high GW variance ranging from the Sahara Desert to the Arabian Peninsula. With the same mechanism, the absence of a meridional wind gradient during the boreal spring equinox season (MA) may result in localized GWs, thus CIPS and AIRS would observe higher GW variances around the GW source over the Equator. The daily zonal wind profiles throughout 2021 over central North Africa in Figure 12e show a wind reversal from weak westward winds at $z < 40$ km to strong eastward winds at $z > 40$ km during MA, and a strong westward stratospheric jet above an altitude of 30 km during MJJA, which supports this hypothesis. However, because the meridional wind gradient is still unknown, this hypothesis requires further investigation based on multi-level observations and numerical simulations.

4.4. Significant GW Hotspots Observed by CIPS Over Other Regions

In the boreal summer season, a large-scale GW hotspot extends from the Bay of Bengal to the Western Pacific (see Figure 4c, 70°E–170°E, 10°N–40°N), and is associated with convective activities in the Asian monsoon anticyclone. Both CIPS and AIRS observe this hotspot during boreal summer. In the PEF hotspots observed by CIPS in Figure 8c, there is a hotspot caused by typhoons over the West Pacific Ocean and monsoon rain belts over the Bay of Bengal and the South China Sea. Due to the towering and huge Tibetan Plateau, the strong land-ocean contrast and orographic relief make the Tibetan Plateau a huge low-pressure center in the boreal summer season and displace the ITCZ to higher latitudes. The northward cool, moist wind from the Indian Ocean is responsible for convective GWs over Bangladesh Bay. As the wind blows around the Western Pacific Subtropical High (WPSH) in a clockwise direction, the northward wind from the Pacific Ocean at the west end of the WPSH meets the cold air mass over the continent and causes precipitation and convective GWs over East Asia, which accounts for the GW hotspot over the South China Sea. Typhoons are firmly connected with GW generation. Based on a case study and simulation of typhoon Saomai in 2006, Kim and Chun (2011) pointed out that GWs exert a positive feedback on tropical cyclone intensification. Hoffmann et al. (2018) concluded that a tropical cyclone at increased maximum sustained wind or intensification stage tends to generate more GW events.

There is also a large GW hotspot over the eastern U.S. during boreal summer, observed by both CIPS and AIRS. Hoffmann and Alexander (2010) and follow-up studies (e.g., de Groot-Hedlin et al., 2017; Stephan et al., 2016) suggested that these GWs are caused by deep convection events such as thunderstorms over the Great Plains, and Atlantic hurricanes over the U.S. East coast and the Atlantic Ocean. On the other hand, the study of Forbes et al. (2022), based on SABER observations, indicates that the source of the hotspot is the Central American Monsoon.

Previous studies based on limb-scanning instruments show a stratospheric hotspot of GW momentum flux centered over the Gulf of Mexico in boreal summer (e.g., from CRISTA Ern et al. (2004), from HIRDLS Alexander et al. (2008), and from SABER for altitudes of 30–50 km, Forbes et al., 2022; Trinh et al., 2018). In the seasonal PEF of CIPS RAA variances, there is a significant GW hotspot centered over the eastern U.S. but a weak GW hotspot that extends over the Gulf of Mexico during boreal summer (Figure 9c). For the PEF of AIRS variances, only the eastern U.S. GW hotspot is present, and no GW hotspot can be recognized over the Gulf of Mexico (Figure 9g). These differences likely arise because limb-scanning instruments resolve a different part of the GW spectrum than nadir imagers like CIPS and AIRS. Nadir-viewing instruments are better at detecting GWs with large vertical wavelengths around the eastern U.S., while the limb-sounding instruments are better at detecting GWs with small vertical wavelengths around the Gulf of Mexico. None of the aforementioned limb observations provide GW propagation directions. Without more detailed information about the GWs such as the horizontal propagation direction vector, one cannot be sure whether they came from Central America or the eastern US. Nadir-viewing instruments like CIPS and AIRS are able to give propagation direction, but ray tracing analysis is still needed to resolve the exact source of each GW event (Perrett et al., 2021).

5. Conclusions and Future Outlook

This article is the first general report of the global GW variance data set derived from the CIPS instrument onboard the Ice in the Mesosphere (AIM) satellite. We present the first near-global seasonal/monthly statistical study of GWs at or just above the stratopause (altitudes of 50–55 km). The GW analysis is based on the CIPS 265-nm Rayleigh albedo radiance measurements obtained under sunlit conditions from April 2019 to March 2022. The CIPS observations resolve GWs with horizontal wavelengths of 20–400 km and vertical wavelengths >15 km. In this article, we also compared AIRS 4.3 μm GW variances to the CIPS data. Monthly and seasonally averaged GW variances and PEFs are derived from both CIPS and AIRS data sets. The GWs are extracted via

FFT analysis of RAA data in each CIPS scene, retaining waves exceeding a noise threshold. Filtered RAA variance is then calculated for each pixel within a 155 km radius. We compute monthly and seasonal GW variances and PEFs on a 0.5° by 0.5° grid after pixels with low SNR are excluded.

We compared the CIPS RAA and AIRS 4.3 μm BT perturbation data sets to assess the relationship between the observations of GWs at two different altitudes, in the middle stratosphere near 30–40 km (AIRS) and near the stratopause/lower mesosphere around 50–55 km (CIPS). Analyses of the monthly and seasonally averaged GW variances and GW PEFs derived from both data sets revealed that most GW hotspots observed by AIRS were also captured by CIPS. Both CIPS and AIRS can observe GWs with long vertical and short horizontal wavelengths, including GWs generated from convection, flow over orography, and the polar vortex. During the solstice seasons, the extratropical stratosphere and lowermost mesosphere are dominated by strong background zonal winds (either eastward or westward), which is preferable for the propagation of GWs with large vertical wavelengths. In the summer hemisphere, there is a three-peak structure in GW variances due to monsoon convection in the subtropics. In the winter hemisphere, the GW hotspots related to the polar vortex jet are seen in mid and high latitudes, and orographic regions (e.g., mountains and islands) induce significant GW variances.

Several GW hotspots that appear differently in the CIPS RAA and AIRS data sets were discussed, especially those displaying distinct characteristics in only the CIPS RAA data set. GW hotspots related to Southern Brazil, the Southern Andes, tropical Africa, and convective regions during boreal summer (i.e., East Asia and North America) were highlighted. The seasonal PEF derived from the CIPS RAA data set shows a hotspot in South Brazil throughout the year, and much more clearly than the PEF derived from the AIRS data set during the non-monsoon seasons. Moreover, the CIPS RAA presents a more significant contrast in the GW activity of different seasons, which may be associated with its higher SNR. Both CIPS and AIRS captured a GW hotspot originating from convection over tropical Africa during the spring equinox season. In the boreal summer season, both instruments also captured a GW hotspot ranging from the Sahara to Arabian Peninsula, consistent with previous observations by nadir-viewing and limb-sounding instruments. A recent study suggests that GWs over this boreal summer hotspot originated from tropical West Africa, but this requires further investigation. Both CIPS and AIRS observe strong GW hotspots in East Asia and North America during the boreal summer. It is noteworthy that the CIPS RAA data set is especially effective in capturing waves related to islands. The higher horizontal resolution enables CIPS to better resolve local maximum GW variances for small stationary sources such as islands, which is promising concerning future work with the CIPS data.

The CIPS RAA generally shows higher variances in the hotspot regions and lower variances in the non-hotspot regions. This can be attributed to either one or a combination of three reasons: (a) CIPS RAA data have a higher horizontal resolution than AIRS 4.3 μm BT perturbation data, so CIPS observes more of the GW spectrum compared to AIRS. (b) CIPS RAA data have higher SNR after the algorithm is applied to filter out noise, so wave signals are less likely to be concealed by noise when deriving GW variances. (c) The magnitude of zonal winds at the stratopause is generally higher than in the stratosphere. Faster winds can enlarge the vertical wavelengths of GWs and make preferable conditions for nadir-viewing imagers on satellites to detect them. Since GW variances of CIPS and AIRS are based on different instruments and different algorithms, there are also other possible reasons (e.g., local time of spacecraft, data coverage and sampling rate, instrument sensitivity related to weighting function) that can contribute to differences between them.

This monthly/seasonal study of global GWs at 50–55 km altitude is based on the CIPS GW variance data set and compared with a similar analysis at lower stratospheric altitudes based on AIRS. The CIPS RAA data set, with its high spatial resolution and high SNR, is well suited for future vertical coupling and GW studies. The work presented here serves as a reference to aid in the selection of regions and seasons of interest for future case studies of stratospheric and stratopause GWs. For researchers who are potential data users, joint observations involving CIPS and other instruments will be useful to study GW coupling mechanisms between different layers in the atmosphere. With more data products processed and accessible for users, statistical analyses based on CIPS RAA data will make more contributions to the climatology of GWs near the stratopause and in the lowermost mesosphere.

Data Availability Statements

CIPS RAA variance data are available from CU-LASP at https://lasp.colorado.edu/aim/download/ (University of Colorado Boulder-Laboratory for Atmospheric and Space Physics (CU-LASP), 2023) and the NASA Space Physics Data Facility at https://spdf.gsfc.nasa.gov/pub/data/aim/cips/ (NASA Heliophysics Space Physics Data

Facility (SPDF), 2023). AIRS data are available from https://datapub.fz-juelich.de/slcs/airs/gravity_waves/data/ (Hoffmann, 2021). MERRA-2 data are available at the Data and Information Services Center, managed by the NASA Goddard Earth Sciences (GES) at https://gmao.gsfc.nasa.gov/reanalysis/ (Global Modeling and Assimilation Office (GMAO), 2015).

Acknowledgments

This work was partially supported by the NASA Small Explorer Program through contract NAS5-03132. S.X. and J.Y. were supported by NSF Grants AGS-1832988, AGS-1651394, AGS-1834222, and by NASA Grants 80NSSC19K0836 and 80NSSC20K0628. C.E.R. also acknowledges NASA Heliophysics Guest Investigator Program Award 80NSSC18K0775. V.L.H. acknowledges support from NASA Grants 80NSSC19K0834 and 80NSSC21K0002. The authors thank Mr. Larry Gordley, Dr. Junhong Wei, and Dr. Joan Alexander for helpful discussions.

References

Alexander, M. J., & Barnet, C. (2007). Using satellite observations to constrain parameterizations of gravity wave effects for global models. *Journal of the Atmospheric Sciences*, *64*(5), 1652–1665. https://doi.org/10.1175/jas3897.1

Alexander, M. J., Gille, J., Cavanaugh, C., Coffey, M., Craig, C., Eden, T., et al. (2008). Global estimates of gravity wave momentum flux from High Resolution Dynamics Limb Sounder observations. *Journal of Geophysical Research-Atmospheres*, *113*(D15), D15S18. https://doi.org/10.1029/2007jd008807

Alexander, M. J., & Grimsdell, A. W. (2013). Seasonal cycle of orographic gravity wave occurrence above small islands in the Southern Hemisphere: Implications for effects on the general circulation. *Journal of Geophysical Research-Atmospheres*, *118*(20), 11589–11599. https://doi.org/10.1002/2013jd020526

Alexander, M. J., Holton, J. R., & Durran, D. R. (1995). The gravity-wave response above deep convection in a squall line simulation. *Journal of the Atmospheric Sciences*, *52*(12), 2212–2226. https://doi.org/10.1175/1520-0469(1995)052<2212:tgwrad>2.0.co;2

Bailey, S. M., Thomas, G. E., Rusch, D. W., Merkel, A. W., Jeppesen, C. D., Carstens, J. N., et al. (2009). Phase functions of polar mesospheric cloud ice as observed by the CIPS instrument on the AIM satellite. *Journal of Atmospheric and Solar-Terrestrial Physics*, *71*(3–4), 373–380. https://doi.org/10.1016/j.jastp.2008.09.039

Baldwin, M. P., Gray, L. J., Dunkerton, T. J., Hamilton, K., Haynes, P. H., Randel, W. J., et al. (2001). The quasi-biennial oscillation. *Reviews of Geophysics*, *39*(2), 179–229. https://doi.org/10.1029/1999rg000073

Blanc, E., Farges, T., Le Pichon, A., & Heinrich, P. (2014). Ten year observations of gravity waves from thunderstorms in western Africa. *Journal of Geophysical Research-Atmospheres*, *119*(11), 6409–6418. https://doi.org/10.1002/2013jd020499

Bosilovich, M. G., Akella, S., Lawrence, C., Cullather, R., Draper, C., Gelaro, R., et al. (2015). MERRA-2: Initial evaluation of the climate. Retrieved from https://gmao.gsfc.nasa.gov/pubs/docs/Bosilovich803.pdf

Carstens, J. N., Bailey, S. M., Alexander, M. J., & Randall, C. E. (2014). The sensitivity of the cloud imaging and particle size experiment to gravity wave density perturbations near the stratopause. In *Paper presented at the AGU fall meeting abstracts*.

Carstens, J. N., Bailey, S. M., Lumpe, J. D., & Randall, C. E. (2013). Understanding uncertainties in the retrieval of polar mesospheric clouds from the cloud imaging and particle size experiment in the presence of a bright Rayleigh background. *Journal of Atmospheric and Solar-Terrestrial Physics*, *104*, 197–212. https://doi.org/10.1016/j.jastp.2013.08.006

de Groot-Hedlin, C. D., Hedlin, M. A., Hoffmann, L., Alexander, M. J., & Stephan, C. C. (2017). Relationships between gravity waves observed at Earth's surface and in the stratosphere over the central and eastern United States. *Journal of Geophysical Research: Atmospheres*, *122*(21), 11482–11498. https://doi.org/10.1002/2017jd027159

Ern, M., Preusse, P., Alexander, M. J., & Warner, C. D. (2004). Absolute values of gravity wave momentum flux derived from satellite data. *Journal of Geophysical Research-Atmospheres*, *109*(D20), 361. https://doi.org/10.1029/2004jd004752

Ern, M., Preusse, P., Gille, J. C., Hepplewhite, C. L., Mlynczak, M. G., Russell, J. M., & Riese, M. (2011). Implications for atmospheric dynamics derived from global observations of gravity wave momentum flux in stratosphere and mesosphere. *Journal of Geophysical Research-Atmospheres*, *116*(D19), D19107. https://doi.org/10.1029/2011jd015821

Forbes, J. M., Ern, M., & Zhang, X. L. (2022). The global monsoon convective system as reflected in upper atmosphere gravity waves. *Journal of Geophysical Research-Space Physics*, *127*(9), e2022JA030572. https://doi.org/10.1029/2022ja030572

Forbes, J. M., Zhang, X., Randall, C. E., France, J., Harvey, V. L., Carstens, J., & Bailey, S. M. (2021). Troposphere-mesosphere coupling by convectively-forced gravity waves during Southern Hemisphere monsoon season as viewed by AIM/CIPS. *Journal of Geophysical Research: Space Physics*, *126*(11), e2021JA029734. https://doi.org/10.1029/2021ja029734

Fritts, D. C. (1982). Shear excitation of atmospheric gravity-waves. *Journal of the Atmospheric Sciences*, *39*(9), 1936–1952. https://doi.org/10.1175/1520-0469(1982)039<1936:seoagw>2.0.co;2

Fritts, D. C., & Alexander, M. J. (2003). Gravity wave dynamics and effects in the middle atmosphere. *Reviews of Geophysics*, *41*(1), 1003. https://doi.org/10.1029/2001rg000106

Garcia, R. F., Doornbos, E., Bruinsma, S., & Hebert, H. (2014). Atmospheric gravity waves due to the Tohoku-Oki tsunami observed in the thermosphere by GOCE. *Journal of Geophysical Research: Atmospheres*, *119*(8), 4498–4506. https://doi.org/10.1002/2013jd021120

Gelaro, R., McCarty, W., Suarez, M. J., Todling, R., Molod, A., Takacs, L., et al. (2017). The Modern-Era Retrospective Analysis for Research and Applications, Version 2 (MERRA-2). *Journal of Climate*, *30*(13), 5419–5454. https://doi.org/10.1175/jcli-d-16-0758.1

Global Modeling and Assimilation Office (GMAO). (2015). *MERRA-2 inst6_3d_ana_Nv: 3d,6-hourly, instantaneous, model-level, analysis, analyzed meteorological fields V5.12.4*. Goddard Earth Sciences Data and Information Services Center (GES DISC). https://doi.org/10.5067/IUUF4WB9FT4W

Gong, J., Wu, D. L., & Eckermann, S. D. (2012). Gravity wave variances and propagation derived from AIRS radiances. *Atmospheric Chemistry and Physics*, *12*(4), 1701–1720. https://doi.org/10.5194/acp-12-1701-2012

Harvey, V. L., Randall, C. E., Goncharenko, L. P., Becker, E., Forbes, J. M., Carstens, J., et al. (2023). CIPS observations of gravity wave activity at the edge of the polar vortices and coupling to the ionosphere. *Journal of Geophysical Research: Atmospheres*, *128*(12), 1369. https://doi.org/10.1029/2023jd038827

Hindley, N. P., Wright, C. J., Smith, N. D., & Mitchell, N. J. (2015). The southern stratospheric gravity wave hot spot: Individual waves and their momentum fluxes measured by COSMIC GPS-RO. *Atmospheric Chemistry and Physics*, *15*(14), 7797–7818. https://doi.org/10.5194/acp-15-7797-2015

Hoffmann, L. (2021). AIRS/Aqua Observations of Gravity Waves [Dataset]. Jülich DATA. https://doi.org/10.26165/JUELICH-DATA/LQAAJA

Hoffmann, L., & Alexander, M. J. (2010). Occurrence frequency of convective gravity waves during the North American thunderstorm season. *Journal of Geophysical Research-Atmospheres*, *115*(D20), D20111. https://doi.org/10.1029/2010jd014401

Hoffmann, L., Alexander, M. J., Clerbaux, C., Grimsdell, A. W., Meyer, C. I., Rossler, T., & Tournier, B. (2014). Intercomparison of stratospheric gravity wave observations with AIRS and IASI. *Atmospheric Measurement Techniques*, *7*(12), 4517–4537. https://doi.org/10.5194/amt-7-4517-2014

Hoffmann, L., Grimsdell, A., & Alexander, M. J. (2016). Stratospheric gravity waves at Southern Hemisphere orographic hotspots: 2003-2014 AIRS/Aqua observations. *Atmospheric Chemistry and Physics*, *16*(14), 9381–9397. https://doi.org/10.5194/acp-16-9381-2016

Hoffmann, L., Wu, X., & Alexander, M. J. (2018). Satellite observations of stratospheric gravity waves associated with the intensification of tropical cyclones. *Geophysical Research Letters*, *45*(3), 1692–1700. https://doi.org/10.1002/2017gl076123

Hoffmann, L., Xue, X., & Alexander, M. J. (2013). A global view of stratospheric gravity wave hotspots located with Atmospheric Infrared Sounder observations. *Journal of Geophysical Research-Atmospheres*, *118*(2), 416–434. https://doi.org/10.1029/2012jd018658

Holton, J. R. (1982). The role of gravity-wave induced drag and diffusion in the momentum budget of the mesosphere. *Journal of the Atmospheric Sciences*, *39*(4), 791–799. https://doi.org/10.1175/1520-0469(1982)039<0791:trogwi>2.0.co;2

Holton, J. R. (1992). *An introduction to dynamic meteorology* (p. 511). Academic Press.

Kim, S. Y., & Chun, H. Y. (2011). Impact of typhoon-generated gravity waves in the typhoon development. *Geophysical Research Letters*, *38*(1), L01806. https://doi.org/10.1029/2010gl045719

Kogure, M., Yue, J., & Liu, H. X. (2021). Gravity wave weakening during the 2019 Antarctic stratospheric sudden warming. *Geophysical Research Letters*, *48*(8), e2021GL092537. https://doi.org/10.1029/2021gl092537

Kruse, C. G., Richter, J. H., Alexander, M. J., Bacmeister, J. T., Heale, C., & Wei, J. (2023). Gravity wave drag parameterizations for Earth's atmosphere. *Fast Physics in Large Scale Atmospheric Models: Parameterization, Evaluation, and Observations*. https://doi.org/10.22541/essoar.167397474.46072527/v1

Lindzen, R. S. (1981). Turbulence and stress owing to gravity-wave and tidal breakdown. *Journal of Geophysical Research-Oceans*, *86*(C10), 9707–9714. https://doi.org/10.1029/jc086ic10p09707

Liu, H. X., Pedatella, N., & Hocke, K. (2017). Medium-scale gravity wave activity in the bottomside F region in tropical regions. *Geophysical Research Letters*, *44*(14), 7099–7105. https://doi.org/10.1002/2017gl073855

Liu, X., Xu, J., Yue, J., Vadas, S. L., & Becker, E. (2019). Orographic primary and secondary gravity waves in the middle atmosphere from 16-year SABER observations. *Geophysical Research Letters*, *46*(8), 4512–4522. https://doi.org/10.1029/2019gl082256

Lott, F., & Miller, M. J. (1997). A new subgrid-scale orographic drag parametrization: Its formulation and testing. *Quarterly Journal of the Royal Meteorological Society*, *123*(537), 101–127. https://doi.org/10.1002/qj.49712353704

Lumpe, J. D., Bailey, S. M., Carstens, J. N., Randall, C. E., Rusch, D. W., Thomas, G. E., et al. (2013). Retrieval of polar mesospheric cloud properties from CIPS: Algorithm description, error analysis and cloud detection sensitivity. *Journal of Atmospheric and Solar-Terrestrial Physics*, *104*, 167–196. https://doi.org/10.1016/j.jastp.2013.06.007

McClintock, W. E., Rusch, D. W., Thomas, G. E., Merkel, A. W., Lankton, M. R., Drake, V. A., et al. (2009). The cloud imaging and particle size experiment on the Aeronomy of Ice in the mesosphere mission: Instrument concept, design, calibration, and on-orbit performance. *Journal of Atmospheric and Solar-Terrestrial Physics*, *71*(3–4), 340–355. https://doi.org/10.1016/j.jastp.2008.10.011

Mcfarlane, N. A. (1987). The effect of orographically excited gravity-wave drag on the general-circulation of the lower stratosphere and troposphere. *Journal of the Atmospheric Sciences*, *44*(14), 1775–1800. https://doi.org/10.1175/1520-0469(1987)044<1775:teooeg>2.0.co;2

McPeters, R. D. (1980). The behavior of ozone near the stratopause from two years of BUV observations. *Journal of Geophysical Research: Oceans*, *85*(C8), 4545–4550. https://doi.org/10.1029/jc085ic08p04545

Meyer, C. I., Ern, M., Hoffmann, L., Trinh, Q. T., & Alexander, M. J. (2018). Intercomparison of AIRS and HIRDLS stratospheric gravity wave observations. *Atmospheric Measurement Techniques*, *11*(1), 215–232. https://doi.org/10.5194/amt-11-215-2018

Miller, S. D., Straka, W. C., Yue, J., Seaman, C. J., Xu, S., Elvidge, C. D., et al. (2018). The dark side of Hurricane Matthew unique perspectives from the VIIRS day/night band. *Bulletin of the American Meteorological Society*, *99*(12), 2561–2574. https://doi.org/10.1175/bams-d-17-0097.1

Molod, A., Takacs, L., Suarez, M., & Bacmeister, J. (2015). Development of the GEOS-5 atmospheric general circulation model: Evolution from MERRA to MERRA2. *Geoscientific Model Development*, *8*(5), 1339–1356. https://doi.org/10.5194/gmd-8-1339-2015

NASA Heliophysics Space Physics Data Facility (SPDF). (2023). CIPS RAA variance data [Dataset]. NASA. Retrieved from https://spdf.gsfc.nasa.gov/pub/data/aim/cips/

Perrett, J. A., Wright, C. J., Hindley, N. P., Hoffmann, L., Mitchell, N. J., Preusse, P., et al. (2021). Determining gravity wave sources and propagation in the southern hemisphere by ray-tracing AIRS measurements. *Geophysical Research Letters*, *48*(2), e2020GL088621. https://doi.org/10.1029/2020gl088621

Plougonven, R., Jewtoukoff, V., de la Camara, A., Lott, F., & Hertzog, A. (2017). On the relation between gravity waves and wind speed in the lower stratosphere over the Southern Ocean. *Journal of the Atmospheric Sciences*, *74*(4), 1075–1093. https://doi.org/10.1175/jas-d-16-0096.1

Plougonven, R., & Zhang, F. Q. (2014). Internal gravity waves from atmospheric jets and fronts. *Reviews of Geophysics*, *52*(1), 33–76. https://doi.org/10.1002/2012rg000419

Randall, C. E., Carstens, J., France, J. A., Harvey, V. L., Hoffmann, L., Bailey, S. M., et al. (2017). New AIM/CIPS global observations of gravity waves near 50–55 km. *Geophysical Research Letters*, *44*(13), 7044–7052. https://doi.org/10.1002/2017gl073943

Russell, J. M., Bailey, S. M., Gordley, L. L., Rusch, D. W., Horanyi, M., Hervig, M. E., et al. (2009). The Aeronomy of Ice in the Mesosphere (AIM) mission: Overview and early science results. *Journal of Atmospheric and Solar-Terrestrial Physics*, *71*(3–4), 289–299. https://doi.org/10.1016/j.jastp.2008.08.011

Sato, K., Watanabe, S., Kawatani, Y., Tomikawa, Y., Miyazaki, K., & Takahashi, M. (2009). On the origins of mesospheric gravity waves. *Geophysical Research Letters*, *36*(19), L19801. https://doi.org/10.1029/2009gl039908

Stephan, C. C., Alexander, M. J., Hedlin, M., de Groot-Hedlin, C. D., & Hoffmann, L. (2016). A case study on the far-field properties of propagating tropospheric gravity waves. *Monthly Weather Review*, *144*(8), 2947–2961. https://doi.org/10.1175/mwr-d-16-0054.1

Trinh, Q. T., Ern, M., Doornbos, E., Preusse, P., & Riese, M. (2018). Satellite observations of middle atmosphere-thermosphere vertical coupling by gravity waves. *Annales Geophysicae*, *36*(2), 425–444. https://doi.org/10.5194/angeo-36-425-2018

University of Colorado Boulder-Laboratory for Atmospheric and Space Physics (CU-LASP). (2023). CIPS RAA variance data [Dataset]. AIM-CIPS. Retrieved from https://lasp.colorado.edu/aim/download/

Vadas, S. L. (2007). Horizontal and vertical propagation and dissipation of gravity waves in the thermosphere from lower atmospheric and thermospheric sources. *Journal of Geophysical Research-Space Physics*, *112*(A6), D19106. https://doi.org/10.1029/2006ja011845

Vadas, S. L., Fritts, D. C., & Alexander, M. J. (2003). Mechanism for the generation of secondary waves in wave breaking regions. *Journal of the Atmospheric Sciences*, *60*(1), 194–214. https://doi.org/10.1175/1520-0469(2003)060<0194:mftgos>2.0.co;2

Watanabe, S., Kawatani, Y., Tomikawa, Y., Miyazaki, K., Takahashi, M., & Sato, K. (2008). General aspects of a T213L256 middle atmosphere general circulation model. *Journal of Geophysical Research-Atmospheres*, *113*(D12), 156. https://doi.org/10.1029/2008jd010026

Wright, C. J., Hindley, N. P., Alexander, M. J., Barlow, M., Hoffmann, L., Mitchell, C. N., et al. (2022). Surface-to-space atmospheric waves from Hunga Tonga-Hunga Ha'apai eruption. *Nature*, *609*(7928), 741–746. https://doi.org/10.1038/s41586-022-05012-5

Wright, C. J., Hindley, N. P., & Mitchell, N. J. (2016). Combining AIRS and MLS observations for three-dimensional gravity wave measurement. *Geophysical Research Letters*, *43*(2), 884–893. https://doi.org/10.1002/2015gl067233

Wu, D. L., & Zhang, F. Q. (2004). A study of mesoscale gravity waves over the North Atlantic with satellite observations and a mesoscale model. *Journal of Geophysical Research-Atmospheres*, *109*(D22), D24106. https://doi.org/10.1029/2004jd005090

Wüst, S., & Bittner, M. (2006). Non-linear resonant wave–wave interaction (triad): Case studies based on rocket data and first application to satellite data. *Journal of Atmospheric and Solar-Terrestrial Physics*, *68*(9), 959–976. https://doi.org/10.1016/j.jastp.2005.11.011

Yue, J., Miller, S. D., Straka, W., Noh, Y. J., Chou, M. Y., Kahn, R., & Flower, V. (2022). La Soufriere volcanic eruptions launched gravity waves into space. *Geophysical Research Letters*, *49*(8), e2022GL097952. https://doi.org/10.1029/2022gl097952

Yue, J., Perwitasari, S., Xu, S., Hozumi, Y., Nakamura, T., Sakanoi, T., et al. (2019). Preliminary dual-satellite observations of atmospheric gravity waves in airglow. *Atmosphere*, *10*(11), 650. https://doi.org/10.3390/atmos10110650